Aeroelastic Optimization of a Helicopter Composite Horizontal Stabilizer Using the Superior Damping Properties of Flax Fibers

Jonas John* Lukas Gaugelhofer* Christoph Hackner** Jack Cumiskey**
Ilkay Yavrucuk***

**Graduate Research Assistant **Master Student ***Professor and Department Head*
Institute for Helicopter Technology and VTOL
Technical University of Munich, 80333 Munich, Germany

Helicopter structures are heavily influenced by vibration, often forcing structural changes late in the design process. While structural dynamics simulations may not always provide accurate results, flight testing remains often the only method to identify dynamic interactions and excitations. This is particularly relevant for new, innovative designs where practical experience is limited. One potential approach to mitigate design risks is to improve the damping of the aircraft structure. Natural fibers such as flax could be a promising approach. However, additional flax material is required to achieve stiffness and strength comparable to carbon components, resulting in increased weight. The aim of this study is to investigate how this weight increase can be minimized while still achieving optimal damping levels. To accomplish this, knowledge gained from the hybridization of simple specimens and cross-sectional laminates has been extended to a 3D laminate configuration. The goal is to develop structures with matching dynamic properties, minimal weight increase, and significant damping improvement. The influencing parameters of this strategy were first tested on double-T beams. High-strain regions were targeted for extensive hybridization to maximize damping, while low-strain regions received minimal hybridization to avoid excessive weight gain. As a practical demonstration, this approach was applied to a horizontal stabilizer. Emphasis was placed on the critical first bending modes, both asymmetrical and symmetrical. The dynamic properties of the structures, including damping and stiffness, were measured by experimental modal analysis. The results illustrate the feasibility of designing hybrid components with comparable dynamic behavior, demonstrating significantly improved damping properties with only a minor increase in weight. For example, the damping in the first symmetrical bending mode of the horizontal stabilizer was more than quadrupled while maintaining the same natural frequency and adding less than 10% of mass.

NOTATION

A	Area of cross section
E	Modulus of elasticity
E_s	Spec. modulus of elasticity
Hy	Hybridisation based on flax fiber content
I	Area moment of inertia
R	Stiffness - damping relation factor
f	Frequency
η	Loss factor
ζ	damping ratio
ρ	Density
UD	Unidirectional

BD	Bidirectional
FEM	Finite Element Method
FRF	Frequency Response Function
HPB	Half-Power Bandwidth Method
ERA	Eigensystem Realization Algorithm
LDV	Laser-Doppler-Vibrometer
CFRP	Carbon Fiber Reinforced Plastics
FFRP	Flax Fiber Reinforced Plastics
DTB	Double-T Beam
CLT	Classical Laminate Theory
SVD	Singular Value Decomposition

1 INTRODUCTION

Vibration is a constant challenge in helicopter development, often causing delays in the development schedule [1]. Several elements of the helicopter, including the primary rotor, tail rotor, engines, and transmission, contribute to the generation and propagation of vibrations. In addition, aerodynamic factors such as rotor and cell wake interactions with the tail boom or empennage can induce structural vibrations. In particular, during periods of low speed and fast forward cruising, aerodynamic perturbations from rotor-fuselage wake and tailboom-empennage interactions induce vibrations [1]. The aforementioned elements are intertwined and closely related, resulting in elevated vibration levels that often require additional vibration mitigation measures such as isolation systems [2] and vibration absorbers [3]. Blade tip vortex interactions with rotor wakes can induce vibrations in tail components [4–6], requiring tailored adjustments to the fuselage, tail structure, or dynamic isolation [5]. Often, modifications are required during the flight test phase, adding cost and extending development time. [7, 8]. Effectively managing these vibration mechanisms and reducing the potential for aeroelastic instabilities is essential to maximize structural damping, thereby reducing both load amplitudes and overall cabin vibration levels. Several approaches exist to improve damping, including the use of elastomeric layer damper concepts [9]. In addition, composite design strategies are exploring the incorporation of viscoelastic materials into laminates and structures [10].

An additional proposal presented in this study is to improve the damping characteristics of helicopter fiber composite structures through the use of natural fibers. These fibers inherently possess significant damping capabilities and therefore offer the potential to improve the overall damping properties of components through a hybrid flax-carbon design [11]. The key advantage is that no additional non-supporting mass is introduced. Thus, this variant offers a unique potential for future aircraft structures.

Flax fibers have found application as structural components in various industries, including the automotive sector. For example, they are used in intricate and high-quality door structures for mid-range and luxury vehicles [12]. It is now being used in skis, in part because of its recognized good damping properties. While progress has been made in understanding the stiffness and failure characteristics of flax materials, for example, in the design of helicopter components such as tail units [11, 13], the use of flax materials in aerospace applications is still in the research phase.

Although some studies have shown promising results, there is still a significant challenge in predicting and optimizing the damping properties of flax materials, especially when integrated with CFRP. For example, Henschel [11] was able to determine higher damping during the manufacture of a flax-carbon hybrid tailplane compared to a reference carbon tailplane. However, her design and investigation did not have damping as an optimization goal, but rather structural stiffness, strength, and a high organic content. The influence of the flax hybrid design specifically on the damping behavior was not part of the study. Therefore, it is necessary to gain further knowledge and predictive capabilities on the damping properties of flax-carbon hybrids, allowing for future applications in the aerospace industry. A first step in this direction was taken by the authors of this paper in a previous study presented at the 48th European Rotorcraft Forum in Switzerland. Here, John et al. [14] were able to quantify the damping properties of different degrees of hybridization and their stiffness-damping relationship. Flax was shown to have a very good damping-stiffness factor of about 2.8 times higher than carbon in the fiber direction. For use in flax-carbon hybrids, it was shown that it is possible to shift the damping-stiffness factor of the laminates in favor of damping by using the correct ply structure.

The damping of the laminates showed a strong dependence on the layup and the distance from the neutral axis of the flax fibers. Therefore, in a next step, John et al. [15] looked at the damping at the structural level and investigated the effect of increased damping on several typical 2D aerospace structures. In this study, it was found that local flax reinforcement in the form of rib structures on shells significantly increases the stiffness damping factor, surpassing simple flax UD0 plates. This makes the use of flax ribs in large area structures very attractive. It was also confirmed that for structures such as double-T beams (DTB), UD0 flax plies in the outer flange are one of the most important factors in improving damping. However, the influence of the ply sequence between carbon and flax became less significant at the laminate level. The study also showed that highly variable laminates with stiff carbon webs and softer flax flanges were less effective than a more uniform laminate structure. Johns' study showed that significant damping improvements can be achieved through hybridization for DTB. Hybridization can result in a three to four times increase in damping. The damping stiffness factor was also significantly increased. For more complex structures like wing sections, high damping was similarly demonstrated.

However, all of the mentioned research has focused on layer substitution, accepting a loss of stiffness in direct comparison. To hybridize a helicopter structure with flax, the resulting components must have the same stiffness and strength as their carbon counterparts. However, due to the lower stiffness of flax, achieving this requires an increase in material and consequently an increase in weight. The present study investigates the extent to which this increase can be minimized while achieving an optimal level of damping of the flax structures. The knowledge gained from the hybridization of coupons and simple laminate cross section configurations will be applied. These findings will be extended to a 3D laminate configuration. The aim is to create structures with equivalent dynamic properties, minimum weight increase and maximum damping improvement. In this context, the aim is to achieve a high degree of hybridization in areas with high strain rates in order to generate maximum damping. In low strain regions, the hybridization should be kept to a minimum to avoid excessive weight increase while maintaining the same stiffness. This approach will be applied and tested on a classical aeroelastically loaded helicopter structure, the horizontal stabilizer. Prior to this, the sensitivities of this approach are tested on a simplified structure, the Double-T Beam (DTB). For both structures, the focus is on the often critical first bending modes, both asymmetric and symmetric.

2 MATERIALS & PROCESS

The current study considered various Flax Fiber Reinforce Polymer (FFRP) materials from different manufacturers. As demonstrated in a previous study by the researchers [16], the mechanical properties of flax products available on the market can vary considerably. This variation includes differences not only in the fibers themselves, but also in the resins and manufacturing techniques used. In particular, prepreg systems have advantageous mechanical properties due to their higher fiber volume content, which makes them easier to manufacture and more manageable. Considering the favorable mechanical properties reported by Gaugelhofer [16], the availability of bidirectional (BD) and unidirectional (UD) material, and the presence of a Carbon Composite Reinforced Polymer (CFRP) prepreg with the same resin system, FIBERPREG® was selected as the manufacturer for the present investigations.

All structures investigated were produced using an autoclave process. The cure cycle was set to the manufacturer's specifications of 120$^{\circ}C$ for 90 min and a heating rate of 2 min/$^{\circ}C$. This, together with an absolute pressure of 6 bar, achieves fiber volume contents of about 50% in the flax composite [14].

The authors have previously examined coupons fabricated from this material to assess their damping and stiffness characteristics at the laminate level. The calculated bending modulus of elasticity E and the loss factors η for low-frequency regions in the fiber direction are presented in Table 1 [14].

Table 1: Material designations and the associated bending module E and loss factor in main fiber direction η_0 determined from [14]

FIBERPREG® PrePreg	E (in GPa)	η_0 ($[-]$)	notation
Carbon C120 UD	73.77	0.21	C
Carbon C200 Twill	39.18	0.302	CT
Flax NAT-120 UD	25.36	1.472	F
Flax NAT-200 Twill	12.62	1.922	FT

3 MEASUREMENT METHODS

The following section outlines the experimental and analytical methods used in this study to determine the damping characteristics of the structures.

3.1 EXPERIMENTAL SETUP

A flexural vibration test was conducted to assess the damping behavior of the bending structures. A distinction was made between two different clamping conditions, a fixed free condition and a clamping condition in a tailplane configuration with two free ends and a clamping in the middle. The experimental setup for tailboom configuration is illustrated in Figure 1. The clamping conditions for each structure are described in their respective chapters.

The Experimental Modal Analysis (EMA) was performed using an impulse hammer for excitation. A laser doppler vibrometer (LDV) was used for non-contact measurement of the velocities of the free end of the beam. Signal analysis and processing was conducted using Simcenter Testlab for precise data acquisition and analysis. Table 2 shows the settings and the specific properties of the obtained data velocity and force.

Table 2: Settings for Experimental Modal Analysis

Scope	Bandwidth	$3200.00 Hz$
	Spectral Lines	65536
	Resolution	$0.0488281 Hz$
	Acquisition time	$20.48 s$
DV	Measured quantity	Velocity
	Electrical unit	V
	Actual sensitivity	$10 \frac{V}{m/s}$
Impact detection	Measured quantity	Force
	Electrical unit	mV
	Actual sensitivity	$2.25 \frac{mV}{N}$

3.2 MEASUREMENT EVALUATION

The frequency response functions (FRF)s were obtained by performing Fourier transformation on the measured velocity and force signals from the impact sensor using SimLab software. The FRF data can be utilized to determine the natural frequencies and the loss factor η_n using the Half-Power Bandwidth Method (HPB), where f_n represents the natural frequency, and f_1 and f_2 are determined as illustrated in Figure 2 [17].

$$\eta_n = \frac{\Delta f_n}{f_n} = \frac{f_2 - f_1}{f_n} \quad (1)$$

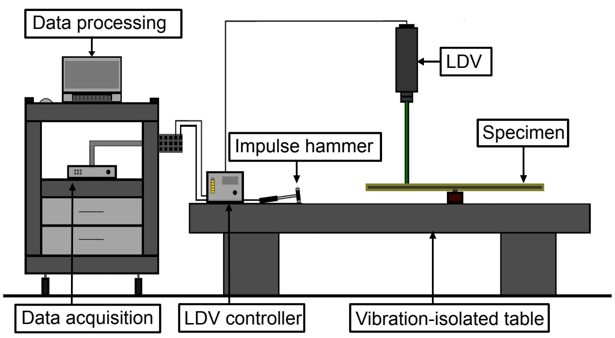

Fig. 1: Experimental setup of the experimental modal analysis (EMA) to determine the frequency response functions. Here, tailplane configuration

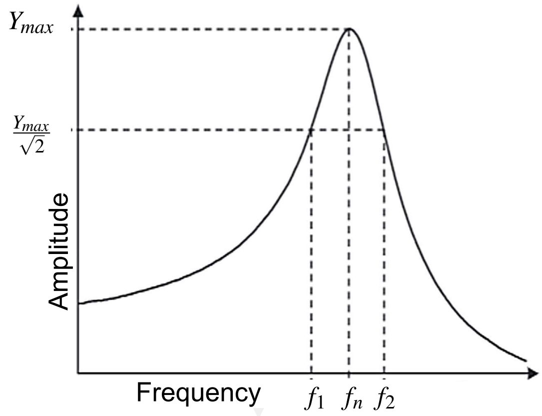

Fig. 2: Visualization of Half-Power Bandwidth method.

For each measurement, the natural frequencies and associated loss factors η_n were determined for the first eigenmode. In case of the tailplane clamping condition in the middle of the structures, the first symmetrical and asymmetrical eigenmode were considered.

Furthermore, the superposition of the investigated modes with parasitic modes has to be considered. The FRFs show not only these two modes, but also several other partially superimposed modes. While the measurement of the specimen oscillations is only in the bending direction, it is not possible to excite the specimens only for these two modes. Theoretically, the excitation of a perfectly manufactured beam, fixed with a perfect clamp exactly in the middle of the flange width, should result in a pure bending deformation. But in reality, the specimen has manufacturing variations, it is not possible to hit the beam exactly in the center with the impulse hammer, and the clamping system can also have imperfections and asymmetries. This leads to the excitation of several other eigenmodes in addition to the flexural ones studied. Since the LDV cannot be perfectly aligned with the centerline of the flange, it can also register deformations caused by these parasitic modes. If the eigenfrequencies of these modes are close to the eigenfrequencies of the investigated modes, this

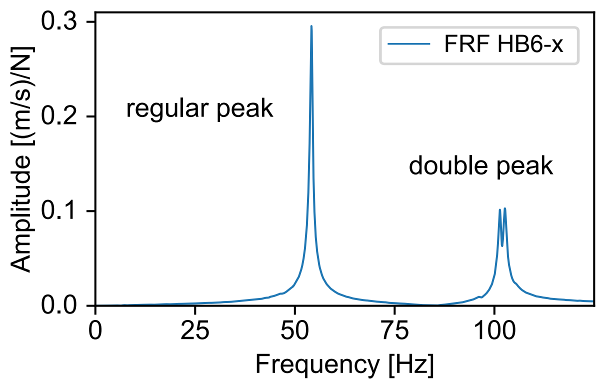

Fig. 3: Example for neglected double peak mode

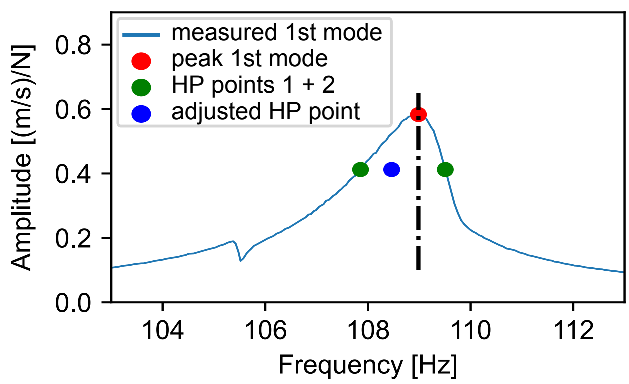

Fig. 4: Loss factor deviation due to close modes

results in superposition, which leads to modifications of the amplitude curves in the frequency domain and thus to incorrect calculation of the eigenmode loss factors. Sometimes this can lead to double peaks, as shown for an example in Figure 3 on a measurement of one of the DTBs. In cases where it was not clearly assignable which peak corresponded to which eigenmode and the two eigenfrequencies were very close to each other, both were not included in the analysis. If it was possible to clearly separate the two peaks from each other, the peak closer to the expected frequency, as measured by other beams, is used to estimate the loss factor, and the other peak is neglected.

Even when the two natural frequencies are clearly separated from each other, the overlap can still influence the damping determined from the HPB. This is demonstrated in Figure 4, where it's evident how the Half Power point is significantly distorted on one side, and the mode does not exhibit symmetrical behavior. While an estimation of the actual damping through a reflection of the unaffected point, as shown in Figure 4, can provide some approximation, it is not sufficiently indicative. In such cases, the Eigensystem Realization Algorithm (ERA), offers a suitable approach and is intended to yield good results even for very closely spaced modes.

ERA is an approach from the field of Operational Modal Analysis (OMA) that allows the extraction from Modal Characteristics from test data. This method is described, among others, in Mohanty [18, 19] and Rex [20] as follows: Modal characteristics that define a system's dynamics, including attributes like natural frequencies, damping ratios, and mode shapes, can be deduced from collected time-domain data through the application of system identification techniques.

A linear system with state vector $\mathbf{u}$, state matrix $\mathbf{A}$, input vector $\mathbf{b}$, and measurement vector $\mathbf{x}$ can be expressed as:

$$\begin{aligned} \mathbf{u}_{k+1} &= \mathbf{A}\mathbf{u}_k + \mathbf{b}_k \\ \mathbf{x}_{k+1} &= \mathbf{C}\mathbf{u}_{k+1} \end{aligned} \tag{2}$$

Here, $\mathbf{C}$ represents the output matrix, and $\mathbf{k}$ is the time index. The identification process involves deriving the system matrix $\mathbf{A}$ from the measurements $\mathbf{x}$. The output measurements at two consecutive time instances are interconnected through the system matrix. To determine the system matrix, the Hankel matrices $\mathbf{H}(0)$ and $\mathbf{H}(1)$ must be computed, starting from $t = 0$ and $t = \Delta t$. Applying the Singular Value Decomposition (SVD) to $\mathbf{H}(0)$ results in:

$$\mathbf{H}(0)_{mp\times q} = \mathbf{U}_{mp\times mp}\mathbf{\Sigma}_{mp\times q}\mathbf{V}^T_{q\times q} \tag{3}$$

In this context, $\mathbf{\Sigma}$ represents a diagonal matrix of singular values, and both $\mathbf{U}$ and $\mathbf{V}$ denote orthonormal matrices of the left and right singular vectors. Furthermore, m stands for the count of output measurements, with p and q representing the number of time instances taken into account within the Hankel matrix. Now define:

$$\begin{aligned} \mathbf{Q} &= \mathbf{U}\mathbf{\Sigma}^{1/2} \\ \mathbf{W} &= \mathbf{\Sigma}^{1/2}\mathbf{V}^T \end{aligned} \tag{4}$$

and the pseudo inverses

$$\begin{aligned} \mathbf{Q}^+ &= \mathbf{\Sigma}^{1/2}[U]^T \\ \mathbf{W}^+ &= \mathbf{V}\mathbf{\Sigma}^{1/2} \end{aligned} \tag{5}$$

The pseudoinverse matrix can be directly computed by performing matrix inversion and multiplication with the square root of the diagonal elements of $\mathbf{\Sigma}$.

If we designate the number of degrees of freedom in the system as N, the dimension of the system matrix becomes $2N$. This results in a set of $2N$ singular values in $\mathbf{\Sigma}$, all of which are nonzero. Hence, the computation of the pseudoinverse matrices follows this pattern:

$$\begin{aligned}\mathbf{Q}_{2N}^{+} &= \mathbf{\Sigma}_{2N}^{-1/2}\mathbf{U}_{2N}^{T} \\ \mathbf{W}_{2N}^{+} &= \mathbf{V}_{2N}\mathbf{\Sigma}_{2N}^{-1/2}\end{aligned} \tag{6}$$

Finally, the system matrix $\mathbf{A}^r$ can be computed:

$$\mathbf{Q}_{2N}^{+}\mathbf{H}(1)\mathbf{W}_{2N}^{+} = \mathbf{A}^r \tag{7}$$

With the help of $\mathbf{A}^r$, now the eigenparameters such as damping can be calculated. The damping ratio, which is half the loss factor η is thus defined with the help of the decay rate λ as:

$$\zeta = \frac{\lambda}{2\pi f} = \frac{\eta}{2} \tag{8}$$

Due to the resource-intensive nature of ERA compared to HPB, ERA was only employed in particularly critical cases with superimposed modes where HPB reaches its limits for predicting accurate damping in order to obtain a better and more general understanding of the data.

4 HYBRIDIZATION APPROACH

4.1 3D HYBRIDIZATION

The purpose of this study is to gain insight into the dynamic behavior of a CFRP-FFRP hybrid helicopter stabilizer. The concept of local fiber substitution is first investigated on DTBs, which also carries the main static and dynamic loads of the horizontal stabilizer used in this study. Figure 5a shows the DTB profile inside the stabilizer. The geometry of a DTB, as shown in Figure 5b , consists of two rectangular flanges, one at the top and one at the bottom, and a web between them. The neutral axis of a beam is the line passing through the centroidal depth of the beam where there is no longitudinal stress, either compressive or tensile, or strain.

The objective of this section is to increase the structural damping of a CFRP DTB by local hybridization with FFRP, while maintaining the eigenfrequencies and eigenmodes of the original structure. This allows the influences of damping optimization through the hybridization strategy to be tested relatively resource-efficiently. The study is

(a) Profile of a tailplane, from [15]

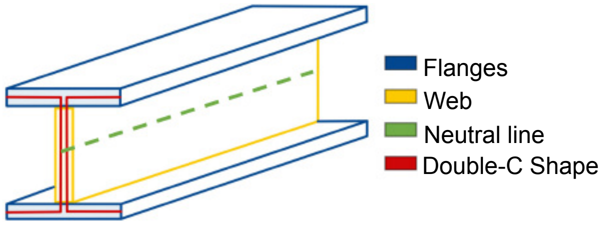

(b) Sketch DTB

Fig. 5: DTB location and nomenclature

limited to the bending eigenmodes of DTB similar to the tail boom of a helicopter. Due to its fixation in the center of the beam, there are two specific eigenmodes addressed in this work: The first symmetrical and asymmetrical bending modes. They are highlighted in Figure 6.

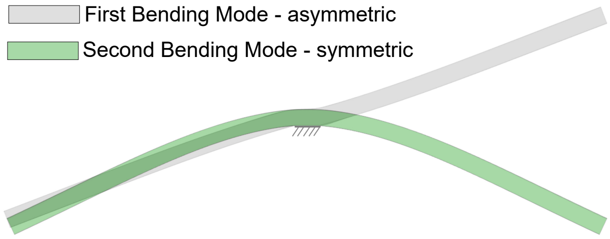

Fig. 6: First two bending modes DTB clamped in the center like tailplane

These eigenmodes correspond to two eigenfrequencies of the system. Figure 7 shows a simplification to a single degree of freedom system consisting of a mass m, a spring with stiffness k, an excitation force $f(t)$, and the position of the mass u. Damping is neglected in this simplification.

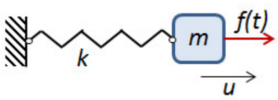

Fig. 7: Undamped system with a single degree of freedom, from [21]

The motion of the mass follows the equation:

$$m\ddot{u} + ku = f(t) \tag{9}$$

In case there is no force f acting externally on the mass, there may still exist nonzero solutions. It can be proved that

$$u = A\sin(\omega_0 t) + B\cos(\omega_0 t) \tag{10}$$

is a solution of the homogenous equation of motion, if

$$\omega_0 = \sqrt{\frac{k}{m}} \tag{11}$$

.

Therefore, the eigenfrequencies ω_0 of the system depend on the stiffness of the spring k and the mass of the system m. The above expression shows in general how stiffness and mass affect the eigenfrequencies [21]:

$$\omega_0 \propto \sqrt{\frac{\text{stiffness}}{\text{inertia}}} \tag{12}$$

This can be applied to the DTBs. The eigenfrequencies corresponding to the bending modes in Figure 6 depend on the stiffness and the mass of the beam. The bending stiffness of a body can be expressed as the product of modulus of elasticity E and moment of inertia I.

In the case of the DTB the modulus of elasticity is derived from the material properties of the beam's body. For composite structures, it can be estimated using Classical Laminate Theory (CLT). A detailed explanation of the concepts of CLT can be found in Giurgiutiu [22]. The moment of inertia can be calculated by adding up the area moments of inertia of the three rectangular sections of the DTB cross-section, the top and bottom flanges, and the web. A detailed explanation of the corresponding calculations is explained in John [15]. The mass m is a result of the geometry of the beam and the density of its constituents.

In conclusion, to achieve the goal of increased damping with similar eigenfrequencies, the beam must be hybridized in such a way that the ratio between stiffness and mass remains the same, while the loss factor of the structure increases. Since stiffness also depends on the moment of inertia I, which depends on the mass, modifying the composite structure of the CFRP by replacing CFRP with FFRP or adding FFRP layers automatically results in a change of both eigenfrequency defining parameters (Eq. 11). Therefore, it is not possible to adjust one of the parameters to compensate for the change in the other. The approach described in this study aims to hybridize the beam while keeping the EI similar. Later, the resulting change in mass and its influence on the eigenfrequencies are evaluated.

The approach is to locally hybridize the beam structures by varying the degree of hybridization along the longitudinal axis of the beam. Due to the strain-dependent damping of flax, the hybrid beam should have a high FFRP content in the high strain regions, while maintaining a high CFRP content in the low strain regions to save weight. Figure 8 shows the high strain regions in the structure of the beam excited to the first symmetrical eigenmode. Here, the elemental strain energy of a FEM model of the DTB is shown. In particular, the inner regions of the flanges are highly strained. In order to achieve higher structural damping, it is hypothesized that the center of the beam must be hybridized with a high content of FFRP that hast to be subjected to strain. Furthermore, this local addition of FFRP results also in an increase in mass, due to the properties of the two constituents (see Table 1). Since the mass increase due to the hybridization is located around the center of the beam, this mass increase is expected to have a small influence on the eigenfrequencies of the beam. This hypothesis will be further explored in the subsequent sections of the paper. The strain mainly affects the upper and lower parts of the beam excited in bending direction. Therefore, in order to better investigate the influences of hybridization in this preliminary study, the focus was initially limited to hybridizing only the flange. This is consistent with John et al. [14, 15] findings that the layers farthest from the neutral axis have a major effect on the damping and stiffness of the structure. However, John et al. [15] also demonstrate that maximum damping potential can only be achieved with a uniformly stiff cross-section, so that the flax fibers can fully exploit their potential. Hence, it is unlikely that the complete damping potential of hybridization can be realized in this initial study. However, the effects

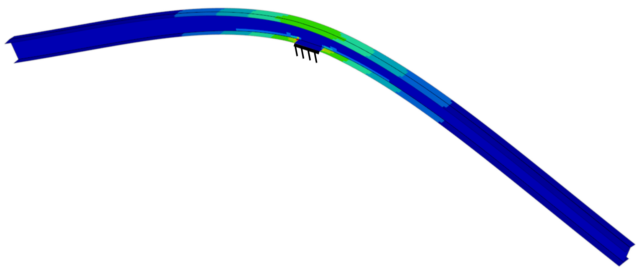

Fig. 8: Element Strain Energy in first symmetrical mode, FEM simulation

of 3D-hybridization can be explored solely in pure bending, avoiding the introduction of extra loading conditions on the flax and maintaining simplicity in the problem.

The objective is now to examine the effects of 3D hybridization that result in optimal enhancement of damping while concurrently minimizing weight. This encompasses parameters such as the flax content across the span, its distribution pattern, and the sequence of layers, that can be investigated on the simplified structure DTB.

4.2 LAYUP PRINCIPLES

There are certain guidelines that should be followed to achieve a sufficient composite structure that influenced the design decisions. This study is based on the directives for the design of composite structures by Schuermann [23].

In the bending modes of the beam, the main direction of tensile stress is longitudinal. According to Schuermann [23] a DTB designed for this type of deformation needs only UD plies arranged in the longitudinal direction of the beam (UD0) to support the normal bending stress. Since a UD0 lay-up of the composite also gives the best results for stiffness to damping [14], the lay-up of the flanges is set to UD0 only for both CFRP and FFRP. However, the web is determined to be a UD0/90 configuration. This means that the UD CFRP plies of the web alternate between a 0° and 90° orientation relative to the neutral line. Due to the manufacturing process the web layers are C-shaped and also contribute to the flanges of the beam as the innermost layers. The assembly of the web and flanges is shown in Figure 9.

The hybridization of the DTB is also performed along the longitudinal axis of the beam. To achieve different ratios of hybridization along the length, the flanges must be made of plies that do not cover the entire length of the DTB. This results in inhomogeneous areas with adjacent sections having different numbers of stacked plies, so-called ply "drop-offs" and "terminated internal plies" [23], shown in Figure 10. These are discontinuities in the laminate and lead to resin pockets that can affect the mechanical properties of the composite structure, for example, by introducing stress concentrations at the drop station [24]. Schuermann [23] gives design guidelines for this type of layup [23]. First, the step size between the layers must be small. If possible, only one layer or a few very thin layers should be

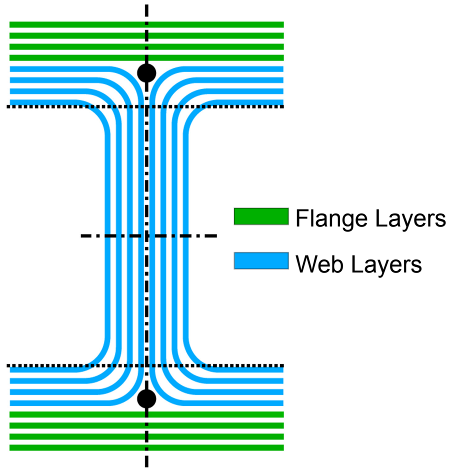

Fig. 9: Assembly of flange and web plies with douple-C shape, edited from John et al. [15]

terminated at once. Second, there must be a sufficient distance between the drop-offs (chamfering). When using UD0 or UD90 plies, the step distance should be at least three times the step size.

An additional design rule for ply drop-offs must be considered. Due to the varying hybridization along the DTB many drop-offs are expected. To avoid high peel stress and structural failure an ending layer should always be covered by another layer [23]. It follows that the outermost layer of the top and bottom flanges should always be the available layer that covers the largest portion of the length of the beam.

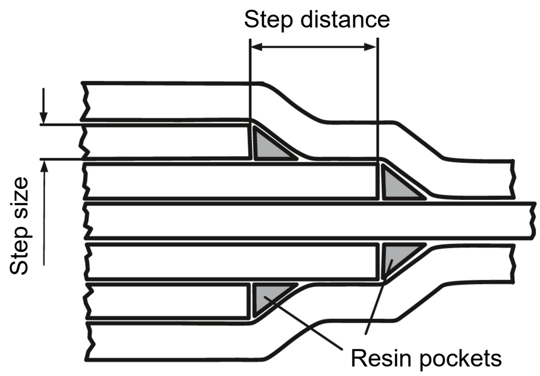

Fig. 10: Terminated internal plies, edited from [23]

4.3 LAYUP GENERATION

The layups of the hybrid beams are determined by an algorithm created for this study. It is designed to configure the layups that satisfy the conditions specified above using CLT. Table 3 shows the required input parameters and the outputs resulting from the code.

The algorithm is based on a reference CFRP DTB that is modified in the process. The notation of the stacked layers is based on John et al. [15]. F indicates a FFRP and C a CFRP layer. The exponent defines the fiber orientation and the index the number of plies. The letter s is short for symmetry. The web layers are numbered from the outside to the symmetry plane and the flange layers are numbered from the inside to the outside.

The flax percentage (FP) describes the ratio of FFRP plies to the total number of plies in the flange over the length of the beam. 100% FP means this section of the flange is all FFRP and 0% FP means that it is all CFRP. Due to the finite layer thickness, it is necessary to define a permissible deviation in the resulting flax content FP and the stiffness EI. To vary the layup in the longitudinal direction, the beam must be divided into a finite number of sections. More sections result in a higher accuracy compared to the desired FP function.

Another parameter required for the layup generation is the size of the clamping in the center. The hybrid beams should be homogeneous in the longitudinal direction within the clamping so that the longitudinal hybridization does not affect the clamping and vice versa. The section covered by the clamping is considered a single section.

The algorithm generates the configuration of the hybrid beam according to the specified inputs. As described the web remains the same as in the reference beam, while the flanges are modified. The top and bottom flanges are assigned a stacking sequence of CFRP and FFRP for each section. Since the sections are not infinitely small, the FP function obtained by the algorithm deviates from the set input parameter. In addition, the EI and mass deviations are compared to the reference beam for each section. The algorithm also determines the layers and their lengths that need to be prepared for the manufacturing process.

Figure 11 shows a flowchart of the algorithm used for the layup generation. In essence, it involves adding or removing layers of CFRP or FFRP and verifying if the specified criteria have been fulfilled.

The required inputs and outputs are listed in Table 3. First, the FP is discretized, the reference beam is divided into the specified number of sections, and the reference beam weight and EI are calculated for each section. Then, the section-wise stacking sequence can be optimized.

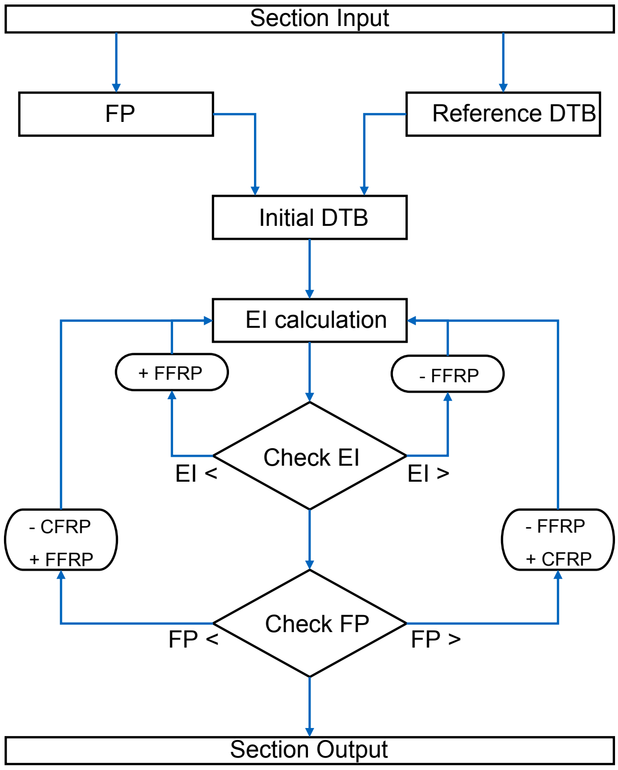

Fig. 11: Layup generation algorithm flow diagram

Since it is not possible to remove or add only part of a layer, there is an edge case in this algorithm. It can happen that the permitted deviation windows of EI and FP are never hit at the same time. In this case, the algorithm pauses after 30 iterations and gradually increases the allowed deviations. Since this study focuses on keeping EI similar, its deviation window is increased only by 0.001 % after 30 iterations while the permitted FP deviation is increased by 0.01 %.

4.4 SPECIMEN DETERMINATION

In order to investigate different ways of hybridizing the DTB, a number of specimens need to be determined, built, tested and evaluated. Some of the possible parameters must be identical for the different specimens in order to compare them. Table 4 shows the constrictions and parameters that remain identical for each hybridized beam analyzed in this study.

The carbon reference beam (RBC) has the eigenfrequencies that all hybrid beams are trying to achieve. Its configuration is the key input parameter of the layup generation algorithm. For this study a CFRP beam with the configuration $[C^0_6/(C^{90}/C^0)_3]$ in the flanges, and $[(C^0/C^{90})_3]_s$ in the web was chosen.

Table 3: Inputs and outputs of the layup generation algorithm

Input	Output
Reference Beam Dimensions	Hybrid Beam Configuration
Reference Beam Configuration	Flax Percentage per Section
Flax Percentage Function	EI deviations to Reference Beam
Permitted Deviation EI	Mass deviation to Reference Beam
Permitted Deviation Flax Percentage	Flange Layers and Sizes
Number of Sections	
Length of Clamping	

Table 4: Input values for the layup generation algorithm

Input	Value
RBC Dimensions	Beam Length $= 860mm$
	Flange Width $= 20mm$
	Web Height $= 23.5mm$
RBC Configuration	Flanges $[C_6^0/(C^{90}/C^0)_3]$
	Web $[(C^0/C^{90})_3]_s$
Permitted Deviation EI	$\pm 5\%$
Permitted Deviation FP	$+5\%$
Number of Sections	83
Length of Clamping	$40mm$

The permitted deviations of EI and FP from the RBC sections are set to be 5% as a consequence of the specific layer thickness. While the hybrid's section deviation is allowed to be + or – 5% of the RBCs EI, the FP deviation window is set to 0 – 5 % to ensure a high flax ratio in the beam. The number of sections is set to 83, resulting in 41 sections on the left, 41 sections on the right, and 1 section covered by the clamping. It is defined by the clamping used in the testing process in this study. Its length is 40 mm. Due to the total length of the beam of 860 mm, this results in a single section length of 10 mm.

The parameters and parameter levels whose effect are examined in this study are listed in Table 5. The first parameter investigated is the FP function. Figure 12 shows the four different functions of interest. According to the design decisions, the highest amount of FFRP should be used in the center of the DTB. The FP functions follow this rule and have a maximum at the center, while the FP decreases as the distance from the center increases. This decline is different for the four functions. According to their names, one decreases in a linear fashion. Two follow a quadratic function, one with positive and one with negative curvature. The fourth function resembles a sinusoidal behavior of FP over the length of the beam. Through this, the impact of the reduction in flax content on damping is intended to be examined.

Table 5: Investigated parameters and parameter levels

Parameter	Parameter Levels
FP function	linear, quadratic+, quadratic-, sinusoidal
Longitudinal extent	full, partial
Hybridization degree	p100, p50
Stacking Sequence FFRP	TD-F, BU-F
Stacking Sequence CFRP	TD-C, BU-C

The extent of hybridization in the longitudinal direction and the degree of hybridization in the flange are examined as two separate contributing parameterss. Full hybridization means that all sections of the beam are part of the hybridization process and are configured in the layup generation algorithm. Partial hybridization limits the hybridization to 50 % of the beam length around the center. The parameter p100 indicates that in the center of the DTB the flange is all FFRP, while p50 indicates a 50/50 ratio of CFRP and FFRP in the center. Figure 13 illustrates the two parameters related to the extent of hybridization for the example of a linear FP function.

The other two parameters investigated are the stacking sequences of the CFRP and FFRP layers. Since the FFRP always sits on top of the CFRP in the flanges, they can be examined separately. TD-F indicates that the FFRP layers are stacked

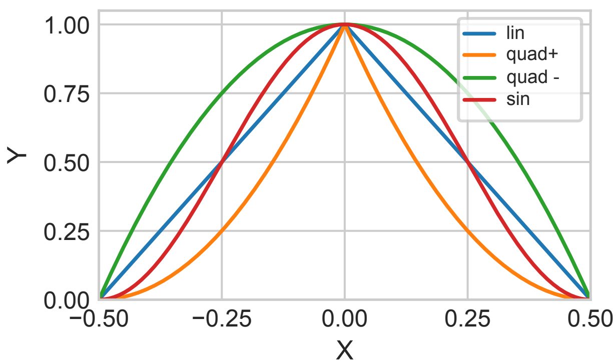

Fig. 12: FP functions

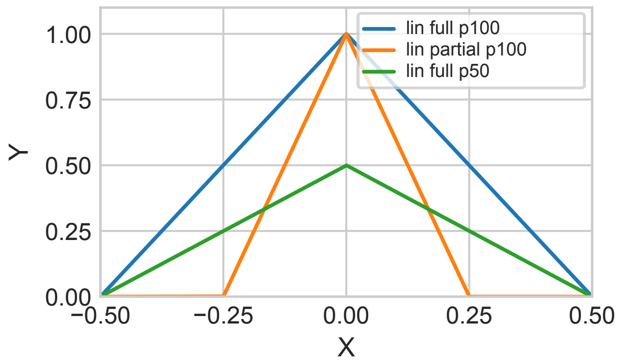

Fig. 13: FP extent and degree of hybridization

in a top down manner meaning that the longest layer is on top and the layers underneath become progressively shorter. BU-F indicates a bottom-up layering of FFRP. TD-C and BU-C are the equivalents for CFRP stacking. The stacking sequences resulting from these orders are then modified according to the rules for ply drop-offs. The BU-F sequence has an additional rule for stacking. The lower layers of the FFRP bulk must be matched to their corresponding CFRP bulk counterparts below. In addition, the longest layer of FFRP must be on top of the layup to comply with layup principles. Figure 14 summarizes the different stacking sequences and the reordering of the layers according to the design rules.

The Matrix Experiment method from Taguchi's Design of Experiments as explained in Klein [25] is used to reduce the number of specimens required in this study. Table 5 shows the parameters and parameter levels for this work. They are suitable for a standard Taguchi field. The Taguchi field used for the specimen determination is the standard $L_8(4^1x2^4)$ field and needs only 8 specimens, as shown in Table 6.

The significant reduction in the number of samples can be seen by comparing it to the number of samples for a standard factorial experiment n_{fac}:

$$n_{fac} = 4 * 2 * 2 * 2 * 2 = 64 \tag{13}$$

In addition to these specimens the RBC and one more hybrid beam are produced. A DTB with a pure FFRP flange (FFB) with a layup that is not aligned to the EI requirement, but optimized to have the same first eigenfrequency as the RBC in a rigid one-sided clamping. This is aimed at achieving the optimal damping for this DTB with a carbon web. Table 7 summarizes the DTB specimens determined to be manufactured for this study. The hybrid DTBs are numbered consecutively with the abbreviation HB.

Table 6: $L_8(4^1x2^4)$ Taguchi Field

Exp.	Factor				
Nr.	A	B	C	D	E
1	1	1	1	1	1
2	1	2	2	2	2
3	2	1	1	2	2
4	2	2	2	1	1
5	3	1	2	1	2
6	3	2	1	2	1
7	4	1	2	2	1
8	4	2	1	1	2

The corresponding FP functions are generated from the individual configurations of the selected beam configurations. These are used to run the layup generation algorithm to determine the layups of the specimens and to estimate the EI and mass distributions and the total beam masses of the DTBs. For example, to achieve the same stiffness EI as 6 layers of carbon in the middle of the flange, 19 layers of flax are required.

4.5 EIGENFREQUENCY ESTIMATION

To confirm that the generated layup configurations have similar eigenfrequencies as the RBC, the first eigenmode and the corresponding frequency of the beams are estimated for a cantilever beam configuration using the Transfer-Matrix method. It enables to determine solutions of the free vibration characteristics of a tapered Bernoulli–Euler beam [26]. It's principle is to discretize a beam with point masses and massless beam segments, as shown in Figure 15. The change of state between these elements is represented by transfer matrices, which form a transfer function between the beam ends. With suitable boundary conditions, solutions to the eigenmodes can be found by iteratively searching for frequencies at which the determinante of the coupled point-mass system is zero.

To compare the hybrid beams with the reference beam, the first eigenmode of the determined beam specimens in cantilever configuration is estimated with this method. Table 8 shows the deviations of the hybrid beams eigenfrequencies to the the RBC value. Except for HB1 and HB3, the calculated eigenfrequencies match the RBC with a deviation of $< 1\%$. As a result, it becomes evident that the increase in mass at the bending root does not significantly influence the natural frequency. Therefore, it is

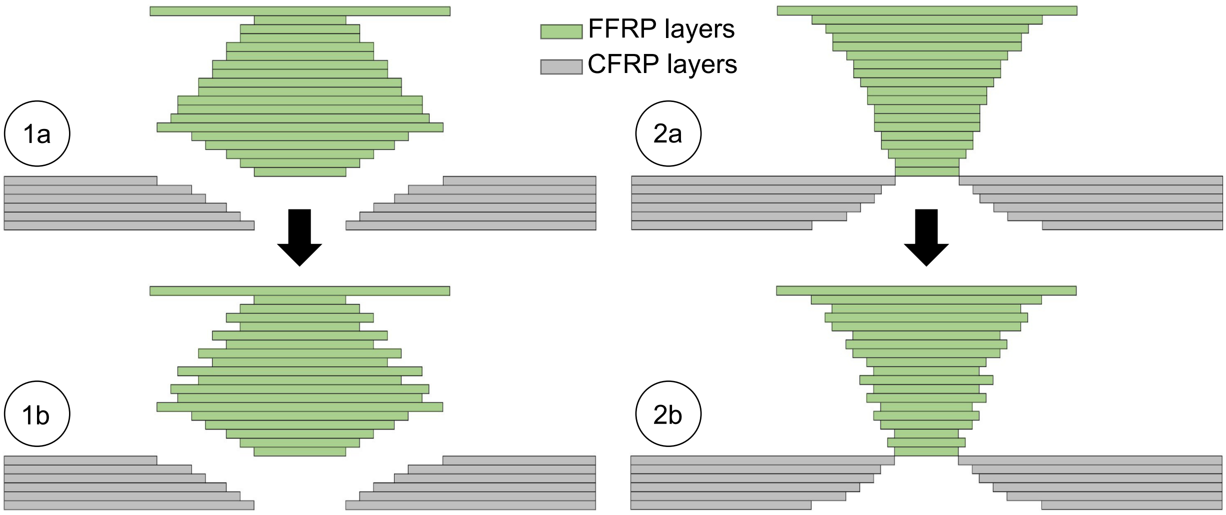

Fig. 14: Stacking sequences of two hybrid flanges, before a) and after b) the modification according to the design rules. 1) shows a BU-F and a BU-C sequence and 2) shows TD-F and TD-C

Table 7: DTB Specimens

Name	Flange				
RBC	$[C_6^0/(C^{90}/C^0)_3]$				
HB1	linear	full	p100	TD-F	BU-C
HB2	linear	partial	p50	BU-F	TD-C
HB3	quadratic+	full	p100	BU-F	TD-C
HB4	quadratic+	partial	p50	TD-F	BU-C
HB5	quadratic-	full	p50	TD-F	TD-C
HB6	quadratic-	partial	p100	BU-F	BU-C
HB7	sinusoidal	full	p50	BU-F	BU-C
HB8	sinusoidal	partial	p100	TD-F	TD-C
FFB	FFRP frequency optimized				

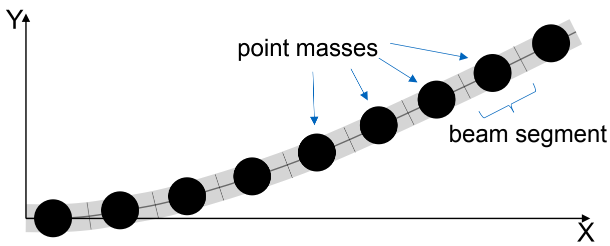

Fig. 15: Discretization in Transfer-Matrix method

reasonable to assume that the EI remains constant along the length of the beam.

The layup of the FFB flange is also generated using the Transfer-Matrix method. The approach for this optimization is to start with a homogeneous full flax flange and gradually adjust it until its estimated eigenfrequency matches that of the RBC. This process results in a flange that has 19 layers of FFRP in the center to mimic the flexural stiffness of the 6 CFRP, but a decreasing number of layers in the outer sections of the beam because the mass farther from the center has an increasing influence on the eigenfrequency of the system. This results to sections with lower EI, but the requirement of maintaining bending stiffness is neglected for the FFB.

4.6 MANUFACTURING & PROPERTIES

A aluminum mold was crafted for the autoclave production process of the double-T beams, ensuring consistent high-quality manufacturing. The mold comprises two C-shaped components and two connectors. The connectors are designed with extended, accurately fitted apertures that enable a linear motion of one C-shaped element towards the other through precision screws. This movement is facilitated by the pressure applied during autoclaving, ensuring uniform web thickness. Post compression and curing in the autoclave, the beams were trimmed to their designated dimensions of width B = 20 mm and length l = 860 mm using a circular saw and a belt sanding machine. The actual beam height and

Table 8: Eigenfrequency validation via Transfer-Matrix method

Beam	$1^{st}\omega_0$ deviation to RBC in %
RBC	0.00
HB1	-3.55
HB2	0.26
HB3	-2.75
HB4	-0.10
HB5	-0.82
HB6	-0.49
HB7	-0.75
HB8	-0.37
FFB	-0.79

web width are dictated by the layer arrangement. The spacing between the two flanges is set at 23.5 mm, a fixed parameter determined by the mold. Figure 16 shows the 10 manufactured DTBs.

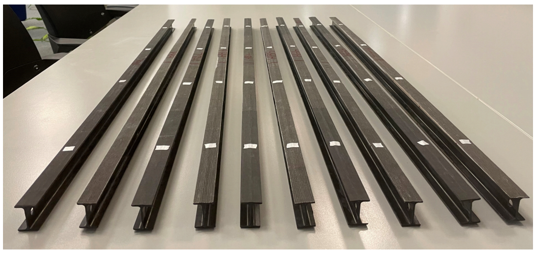

Fig. 16: All 10 manufactured DTBs. RBC, HB1-8 and FFB

The precise dimensions were gauged and averaged across nine points over the span. Figure 17 shows the flange thickness of the DTBs compared to the design thickness based on the manufacturer's specification.

The mean deviation of 12.64 % indicates that not as much resin outflow occurred during the cure cycle as in the manufacturer's material specification tests, resulting in thicker layers. A large difference can be seen especially in the center of the beams with a P100 configuration, where the deviations of numerous layers add up to a significant difference.

The layup generation algorithm also estimates the mass distribution and total mass of the beams using the layup and the density of its constituents. Because the distribution of mass cannot be measured without cutting the beam into pieces, the mass difference is evaluated using the total beam mass. Figure 18 compares the targeted total mass estimated by calculation and the measured mass from the manufactured beams.

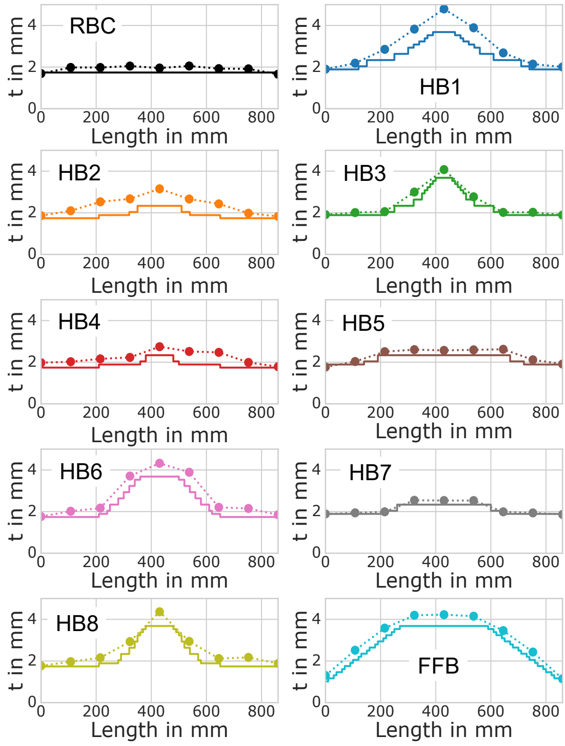

Fig. 17: Measured flange thickness after postproduction compared to calculated thickness according to the manufacturer's specifications used in the design

With the exception of HB1 and HB7, all beams are heavier than expected from the calculation. This is again due to the difference in cured ply thickness between the manufacturer's specification and the thickness achieved in this study. Because the plies are thicker than specified in the data sheets, they store more cured resin and are therefore heavier. HB1 and HB7 should also resemble this deviation. However, due to post-production process, more material was removed from the flanges, making the two beams lighter than their target dimensions would suggest.

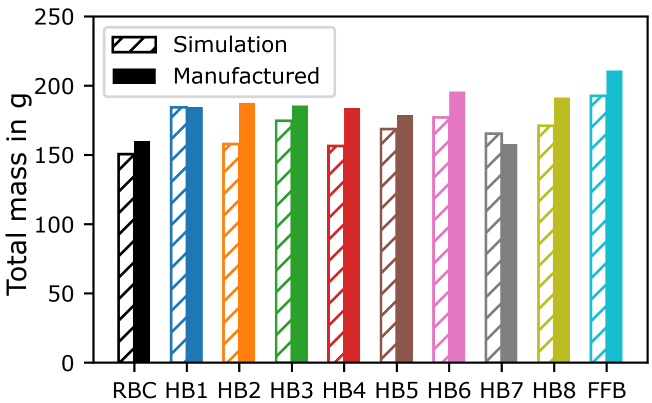

Fig. 18: Measured total beam mass of the DTBs and calculated mass from layup generation algorithm

4.7 DYNAMIC ANALYSIS

4.7.1 Clamping Condition & Test Procedure

To examine the achieved damping, the method described above for determining natural frequencies and modal damping using the EMA and HPB was employed. The DTBs were tested under two conditions: centrally clamped with symmetric free ends (tailplane condition), and with a fixed clamping on one side at the center.

4.7.2 Tailplane Condition

Figures 19a and 19b show the experimental setup of the first series of tests. A clamping block is mounted on a vibration-isolated table. It carries a device consisting of a steel base plate and two steel jaws. The DTB is placed symmetrically in the center and one flange is clamped from both sides by the jaws. To ensure proper distribution of the clamping force, stainless steel sheets are placed under the jaws to mimic the thickness of the beam flange. The clamping system screws are all tightened to the same torque of 15 Nm. The LDV is mounted on a traverse on the ceiling at a distance of 1.7 m and pointing on the top of the DTB. Four measuring points are marked with reflective tape on each flange at distances of 107.5 mm and 322.5 mm to the left and right of the beam center. The designation of the spots is shown in Figure 20.

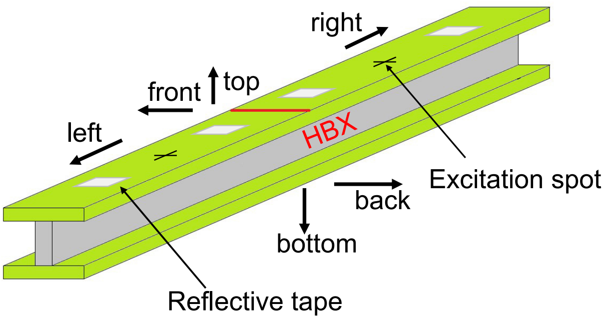

Fig. 20: Spots for excitations and measurements

Eight measurements, four on the top flange and four on the bottom flange, are taken at the marked locations. The DTBs are excited with an impulse hammer at 215 mm from the center on the same side as the laser measurement. In addition, a weak excitation measurement is performed on the top left out spot and on the top right out spot a measurement with the excitation on the left side of the beam is

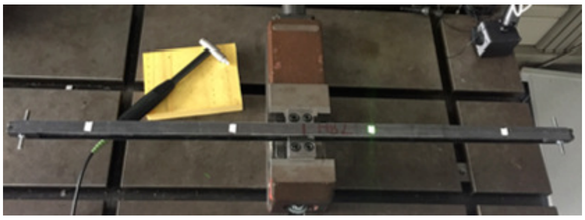

(a) Clamped DTB

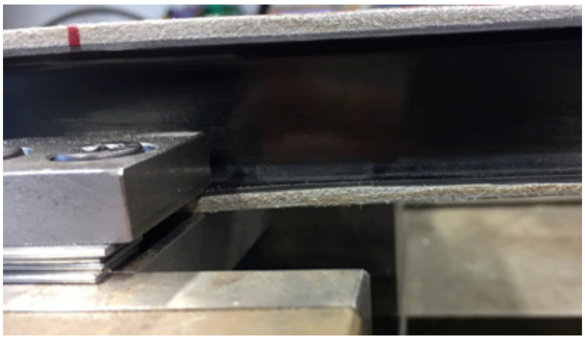

(b) Clamping system

Fig. 19: Images from tailboom clamping test series

conducted. The measurements always record the averaged FRFs of three hits with the impulse hammer. Table 9 shows the ten measurements taken for each beam.

Table 9: Measurement plan for tail boom test series, repeated for all DTBs

Test Nr.	Orient. (upside)	Meas. Side	Meas. Position	Excit. Side	Excit. Force
1	top	left	outside	left	weak
2	top	left	outside	left	strong
3	top	left	inside	left	strong
4	top	right	inside	right	strong
5	top	right	outside	right	strong
6	top	right	outside	left	strong
7	bottom	right	outside	right	strong
8	bottom	right	inside	right	strong
9	bottom	left	inside	left	strong
10	bottom	left	inside	left	strong

4.7.3 Testseries: Cantilever Beam

In the second series of tests, the DTBs are investigated in a free-clamped boundary configuration, as shown in Figure 21. Again, a clamping block is mounted on a vibration-isolated table. It clamps the flanges of the beam so that only one side of the beam is cantilevered. A clamp support ensures that the beams are securely fixed and that the clamping mechanism does not bend the web structure. The uniform section in the center of the DTB is secured inside the clamping and provides a straight surface for the clamping jaws to sit on. The LDV is mounted on a tripod at a distance of 2 m and pointed at the flange of the beam. The measuring point is marked with reflective tape at a distance of 302.5 mm from the clamping. In this series, the beams are also excited with an impulse hammer. The flange to which the laser is directed is struck 10 mm from the clamping. Again, the measurements record the averaged FRFs from three separate hits. Both sides of the DTB were measured and excited.

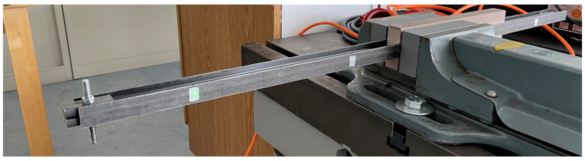

Fig. 21: One-sided clamping

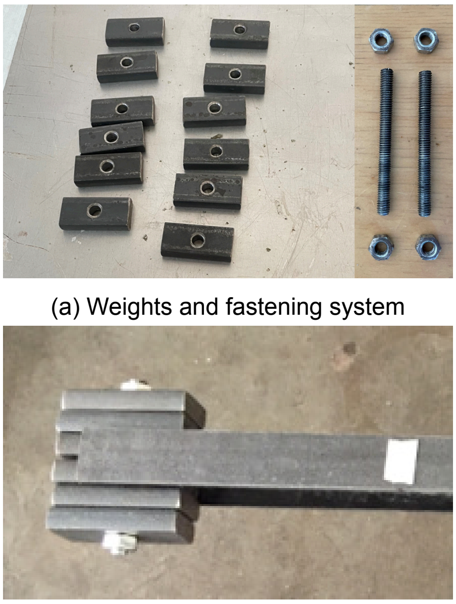

(a) Weights and fastening system

(b) Attachment on beam end

Fig. 22: Additional weights

4.7.4 Frequency Tuning

To also investigate low frequency eigenmodes and the influence of additional mass, the beams are also tested with different weights attached to the ends. These weights simulate beam strain with CFRP and provide results for different eigenfrequencies so that the damping-frequency relationship can be investigated. For this purpose, 12 identical steel weights with an average mass of 49.2g are fabricated. They are attached symmetrically to the DTBs using holes drilled in the beam ends, threaded bolts and nuts. Figure 22 shows the weights and their attachment to a beam end. The mass of a single fastening system of one bolt and two nuts is 15,1g. This results in four different test weight classes, as shown in Table 10. All the described test combinations have been measured using the different weight combinations.

Table 10: Weight classes for testing

Label	Additional weights	Added mass (left + right)
0G	none	$0g + 0g$
1G	2 bolts, 4 nuts, 4 weights	$113.5g + 113.5g$
2G	2 bolts, 4 nuts, 8 weights	$211.9g + 211.9g$
3G	2 bolts, 4 nuts, 12 weights	$310.3g + 310.3g$

4.7.5 Results

The results for the loss factor versus the frequency of the cantilever test series are shown in Figure 23. The black markers and corresponding dotted lines mark the reference beam characteristics measured in that configuration. While the eigenfrequencies of the first mode in this configuration are close to the RBC eigenfrequency, the loss factor of each hybrid DTB is higher than that of the RBC in each weight class. In weight class 0G with no additional weights, the eigenfrequencies and loss factors vary considerably compared to the other weight classes. Once an additional weight is added, the frequency of the mode drops to less than half the eigenfrequency of the beam without additional weights. The results for HB3 with 0G weight class are neglected and not displayed because the FRFs showed a double peak in the corresponding measurements.

The deviations in the natural frequencies of the beams compared to the reference beam in this fixed-end configuration are notably small. On average, the deviation is only 2.5%. The largest deviation is observed in the case of the FFB, at around 5%. This correlation is consistent with the calculations performed using the transfer matrix method, and confirms the assumptions made about designing dynamic characteristics through a direct comparison. This indicates that the EI of the hybrid DTBs is slightly higher than the target EI of the RBC. As mentioned above, the flanges of the manufactured DTBs are thicker than previously estimated. Applied to the composite layup, this results in thicker FFRP and CFRP layers, indicating that the individual stacked layers are further away from the neutral line than previously calculated. The increase in distance is

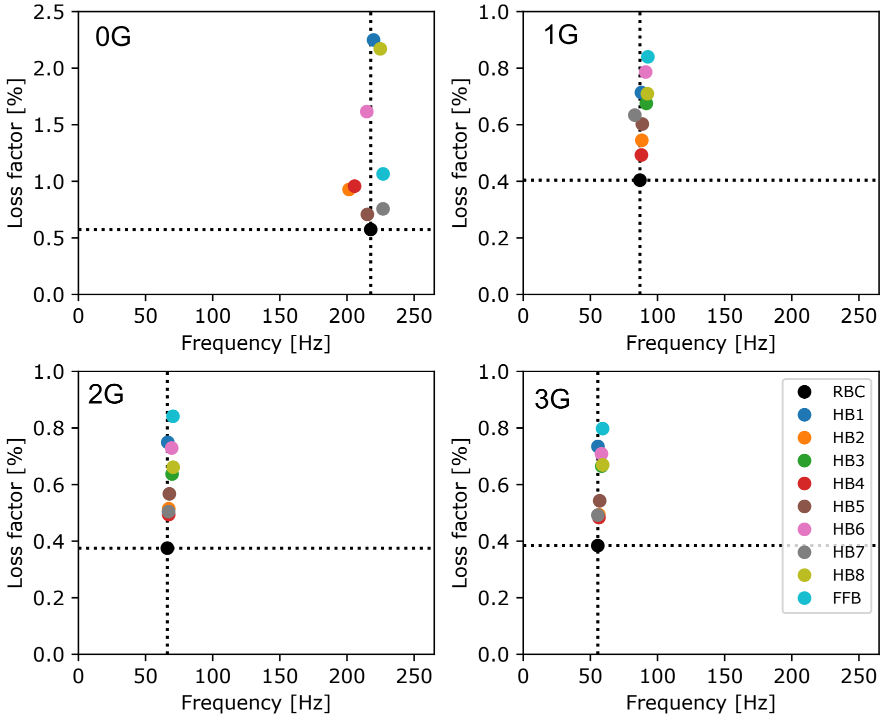

Fig. 23: Loss factors and eigenfrequencies obtained from cantilever test series for the different weight classes 0G, 1G, 2G and 3G

cubically included in the Steiner part of the moment of inertia calculation. Therefore, I and EI are higher in the manufactured DTB and the eigenfrequencies are shifted. In the layup generation algorithm, the permitted deviation for the EI was set to 5%. Applying this deviation to equation 12 yields the permitted deviation of the eigenfrequency results to be 2.5 %. The average deviation for all beams in the cantilever configuration is approximately 2.4%, which meets this requirement.

$$\omega_0 \propto \sqrt{\frac{1{,}05 * \text{stiffness}}{\text{inertia}}} = 1.025 * \sqrt{\frac{\text{stiffness}}{\text{inertia}}} \qquad (14)$$

Except for 0G, the damping behavior shows a very similar pattern for all different weight classes. For all hybrid beams, the damping is higher compared to the reference beam. In addition, there's an observable pattern in the hierarchy of damping levels. In the 1G, 2G, and 3G weight classes, the beam with a 100% flax flange displays the highest damping. The damping of the pure carbon beam RBC is also comparable to the pure carbon beam results of John et al. [15] who determined a loss factor of about 0.33% for a similar but thinner full carbon beam with varying end conditions, providing a basis for comparison.

Figure 24 presents the collected results for the tail boom test series. The average eigenfrequencies and corresponding loss factors of all measurements are shown separately for each weight class. Each figure shows two sets of points. The corresponding modes are determined by FEM analysis. The lower frequency bulk resembles the first eigenmode, the asymmetrical one, and the higher frequency bulk resembles the second bending eigenmode, the symmetrical one.

Unfortunately, the HPB results of the RBC's asymmetrical mode are strongly affected by a nearby peak, as described above. For this reason, it was decided to determine the attenuation using the Eigenvalue Realization Algorithm (ERA) method for comparison. The ERA results are shown here in a diamond shape and were used as a reference for all asymmetrical mode results. Additionally, an estimate of the attenuation for the RBC was made using the HPB method based on a symmetrycal estimate. These points are marked with crosses. Comparing these three methods, it is clear that the results are quite different and vary significantly across different weight classes. The damping for 2G and 3G remains relatively constant with the ERA method. However, the values for 0G and 1G vary considerably. For 0G, the damping of the RBC according to ERA is significantly lower than all comparison beams, while for 1G it is higher. Therefore, the results for the attenuation of the asymmetrical modes due to the

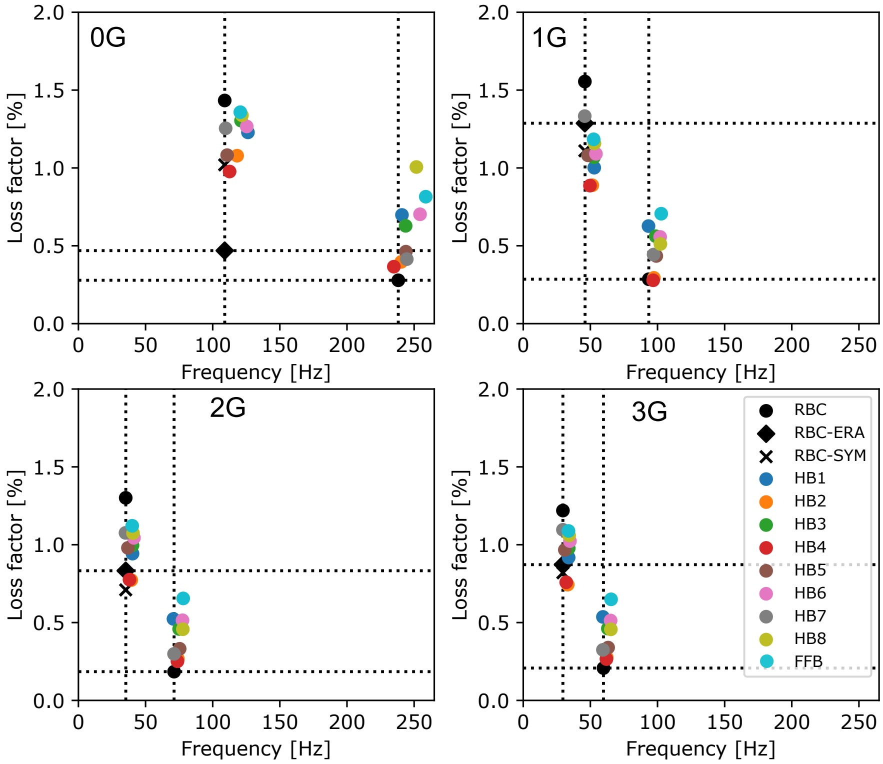

Fig. 24: Loss factors and eigenfrequencies obtained from tailplane test series for the different weight classes 0G, 1G, 2G and 3G

influence of the nearby mode are of limited use. In general, the loss factors of the asymmetrical modes of the DTBs vary more among themselves.

Nevertheless, this is not true for the symmetrical bending mode. Here, the damping ratios remain relatively constant across the beams, even though the damping diminishes as the tuning mass increases. It is evident that the order of damping levels consistently follows the same pattern, resulting in two distinct groups. HB2, HB4, HB5, and HB7 consistently exhibit lower damping compared to the other hybrid beams. The beam with the pure flax web, FFB, consistently demonstrates the highest level of damping, excluding the 0G case where HB8 exhibits the highest damping in the symmetrical mode. Generally, the dispersion is highest for the 0G case. Viewed as a whole, the pattern of the damping between the paper is also apparent in the asymmetrical mode, though not as consistent and with variations, especially concerning the reference beam RBC.

Regarding the natural frequencies, it is noticeable that they are similar for all cases of the symmetrical mode. The maximum deviation is less than 10% (FFB) and on average, not exceeding 5%. For the asymmetrical mode, the mean deviation is slightly higher, but still not exceeding 12%.

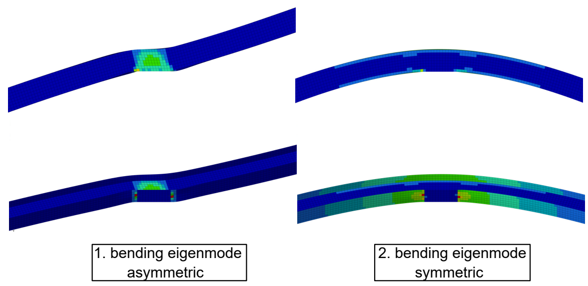

Fig. 25: Elemental strain energy in the first two bending eigenmodes in FEM

In the obtained results the asymmetrical mode show a significantly higher damping than the symmetrical one. The difference is about a factor of 2. Figure 25 gives a possible reason for this unexpected difference. FEM simulations of the asymmetrical and symmetrical modes are depicted, highlighting the elementary strain energies in the model. It can be observed that the strains in the symmetrical mode are as expected, mainly in the flanges. However, in the asymmetrical mode, the strains are not mainly in the flanges, but in the web above the clamp. Since the DTBs are only fixed at the center of one flange, the clamp allows for shear in the web. While the second mode does not induce high shear stresses due to the symmetry of the motion, the

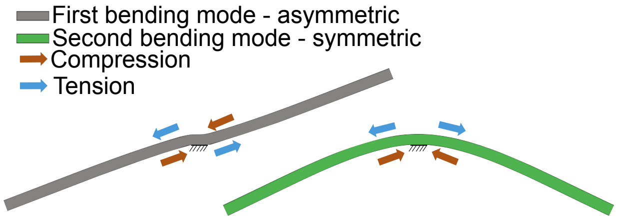

Fig. 26: Tension and compression forces in tail boom test series

motion of the first mode induces shear deformation of the web. The resulting strains have a profound effect on the damping properties. Since the web is identical for all DTBs, the resulting deviations from the RBC loss factor can still be attributed to the hybridization of the flanges.

An additional factor causing these unexpectedly high results may be the quality of the clamping and the forces acting on it. The eigenmodes induce tension and compression forces around the clamp, as shown in Figure 26. For the symmetrical eigenmode they cancel each other out, but for the asymmetrical one they accumulate. If the beam is not sufficiently fixed, this can lead to movement of the beam relative to the fixture and thus increase friction losses between the flange of the DTB and the clamping system. This friction increases the energy dissipated during vibration and thus, the loss factor. Overall, the quantitative damping results of the asymmetrical mode should be interpreted with certain limitations. However, qualitatively, an increase in damping with higher flax content and a similar influence of various hybridization strategies can still be observed.

In previous studies by John et al [15] a relationship between loss factor and frequency for longitudinally homogeneous DTBs was discovered. He found that the damping characteristic increases linearly with frequency. This relationship is also examined for the 3D-DTBs investigated in this study. Figure 27 shows the average loss factors obtained from the tailplane test series for all DTBs at their corresponding eigenfrequencies, for the first and second bending eigenmodes. It is evident that, in this study as well, damping generally increases with frequency. This effect is more pronounced for the asymmetrical mode than for the symmetrical mode. Figure 27 also clearly illustrates the outliers in the measurements. Particularly in the 1G configuration (the third point in the series of four) stands out. Notably, the HB7 beam and the carbon beam, as well as HB8 at the highest frequency, deviate significantly from the pattern.

Figure 28 illustrates the loss factors averaged over all weight classes as deviations in comparison to

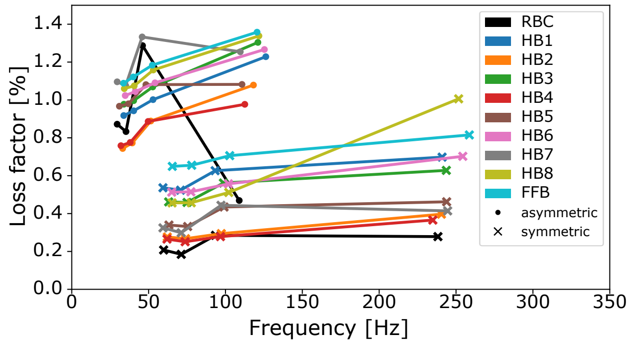

Fig. 27: Loss factor - frequency relation in tailplane clamping test series

the average loss factor of the RBC. The consistent pattern seen in individual weight classes is also mirrored in the average damping results. The highest increase in damping is observed for FFB with the 100% flax flange, followed by HB1, HB3, HB6, and HB8 in the symmetric mode. A factor of up to 2.5 is achieved compared to RBC. In the asymmetrical mode, the increase in damping is not proportionally. The absolute damping values are significantly higher. Nevertheless, when looking at the absolute differences in damping, they remain within a similar range and are only slightly lower for HB3, HB5, HB6 and HB8. This could also be attributed to the inadequate damping detection capabilities of this RBC mode. Given the significant deviations in the RBC values, it suggests that the actual damping of the beam might be lower than determined. However, it's worth noting that the average values for HB1 and HB7 in the asymmetrical mode also exhibit deviations when compared to those in the symmetrical mode.

To comprehensively examine the effects of the differences among the DTBs, the studies were structured using a matrix experimental approach from Taguchi's Design of Experiments. The loss factor results for the different eigenfrequencies are evaluated according to this method. Only the tail-boom test series is considered for this evaluation, and the results for weak and other-side excitation are neglected. Because of the different influences of flanges and webs on the damping properties of the different eigenmodes, the method is performed separately for the asymmetrical and symmetrical eigenmodes.

Taguchi employs the unit dB as a comprehensive physical measure, as discussed by Klein [25]. The fundamental issue revolves around maximization. The optimization function used to convert the loss factor outcomes of the two modes into the decibel domain is presented in Formula 15.

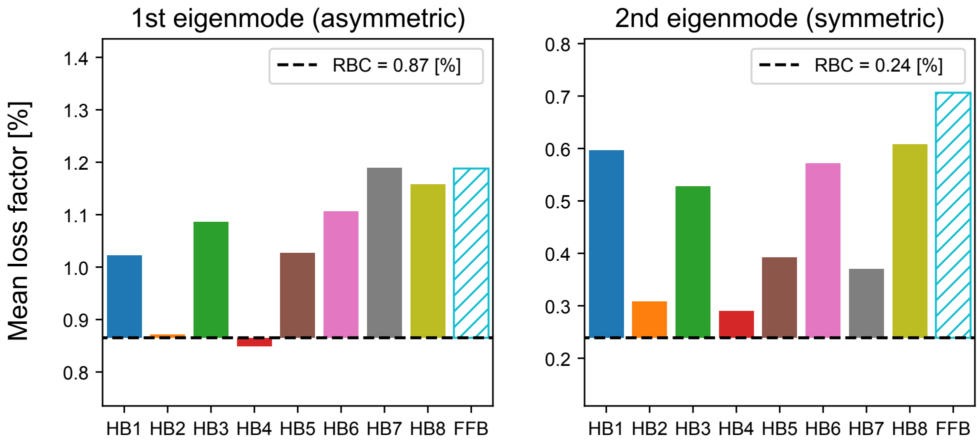

Fig. 28: Mean loss factors of hybrid DTBs for first two bending eigenmode in comparison to RBC

$$\eta_{dB,i} = -10\ \log_{10}(\frac{1}{G}\sum_{i=1}^{G}\frac{1}{\eta_i^2}) \quad (15)$$

η_i are the loss factors of the beams and G is the number of inspected weight classes. $\eta_{dB,i}$ is the resulting value for the DTB specimen in dB. Table 11 displays the absolute loss factors of each hybrid beam and the transformed values in dB.

Table 11: Mean loss factors of HB1-8 and transformation in decibel domain

Beam	η_{asym}	$\eta_{asym,dB}$	η_{sym}	$\eta_{sym,dB}$
HB1	1.02	0.03	0.60	-4.7
HB2	0.87	-1.47	0.31	-10.5
HB3	1.09	0.56	0.53	-5.78
HB4	0.85	-1.55	0.29	-11.0
HB5	1.03	0.20	0.39	-8.41
HB6	1.11	0.79	0.57	-5.06
HB7	1.19	1.40	0.37	-8.98
HB8	1.16	1.16	0.61	-5.56

The effect of a parameter level is the mean deviation from the arithmetic mean caused by it. To evaluate it, the signal to noise ratio S/N of each parameter level is calculated and illustrated in Figures 29 and 30. Since the absolute loss factors are higher in the asymmetrical mode than in the symmetrical mode, the transformed values in the decibel scale are also higher. For the analysis of means, however, only the deviations from the arithmetic mean of the loss factors of all HBs are relevant.

The values of the levels corresponding to a parameter are connected and the parameters are separated by vertical dotted lines. The arithmetic mean of the eight samples is represented by a horizontal dashed line. Values above the arithmetic

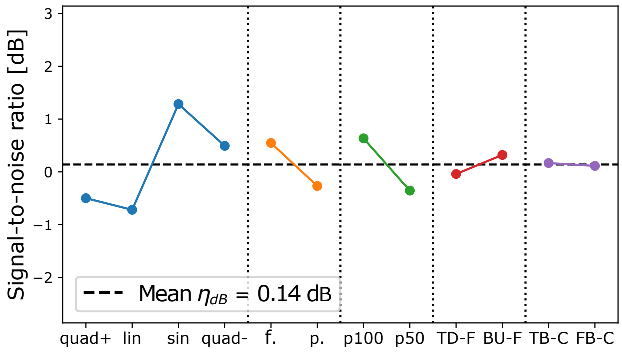

Fig. 29: Matrix experiment evaluation with analysis of means for asymmetrical mode

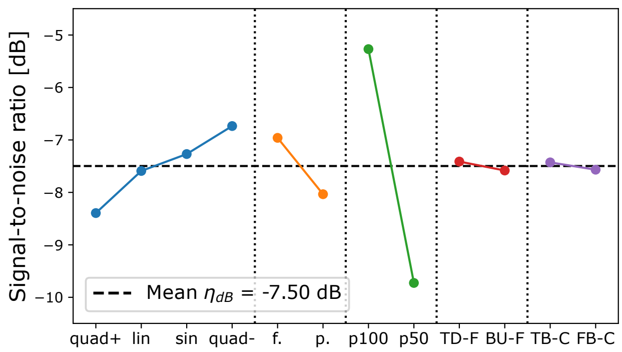

Fig. 30: Matrix experiment evaluation with analysis of means for symmetrical mode

mean indicate a positive contribution of the specified parameter level, while values below the arithmetic mean indicate a negative effect on maximizing the design criterion loss factor. Figures 29 and 30 show which Parameter levels tend to give better results for the loss factor. For the FP function, the downward opened parabola ("quad-") and the sinusoidal function ("sin") provided better results than the "lin" and "quad+" functions for both the asymmetrical and the symmetrical mode. While the sinusoidal function improved the loss factor of the asymmetric mode the most, it had less effect on the symmetrical mode compared to the ”quad-” function. Since the results of the asymmetrical mode depend on several other factors besides the hybridization of the flanges, the influence of the FP distribution can be better evaluated by the results of the symmetrical mode. In 30, the FP function levels are displayed in order of the rate at which the FP decreases from the center. The fastest decrease is observed with the ”quad-” function and the slowest with the ”quad+” function, see figure 12. The results show that the slower the descent in FP, the greater is the loss factor.

For the degree of hybridization parameter, better results were obtained for the ”full” parameter level, hybridization over the entire beam length, for both modes. The degree of hybridization had a better effect when using the ”p100” configuration than the ”p50” for the asymmetrical mode and a significantly higher effect for the symmetrical mode. The stacking order of the FFRP and CFRP layers has a small effect on the loss factor compared to the other parameters. However, it is noticeable that the stacking order of the FFRP layers has an inverse influence on the asymmetric and symmetrical eigenmode.

Table 12 summarizes the conclusions that can be drawn from the evaluation of the matrix experiment and highlights which parameter levels tend to yield better results. The best loss factor results are expected for a DTB hybridized with either the ”quad-” or ”sin” function over the entire beam length and flange thickness. Since the damping of the asymmetrical mode is also highly dependent on the web of the DTB, the stacking order of the FFRP should be optimized for the symmetrical eigenmode and therefore in a ”top down” configuration as well as the CFRP stacking order.

The increase in damping due to the hybrid structure is always countered by the resulting additional weight. To be competitive with other damping methods, the increase in weight must always be considered in relation to the increase in damping. the mass-gain/loss factor-gain relationship is examined. Figure 31 shows the average increase in loss factor in % over the increase in beam mass in % for all hybrid DTBs in the tail boom test series. The two lines represent the linear fit calculated across all beams for each respective mode. The mass of the beam is directly correlated with the degree of hybridization. If a point lies above the line, it indicates that for this beam hybridization led to a particularly weight-efficient increase in damping. Comparing the two modes, it’s evident that the asymmetrical

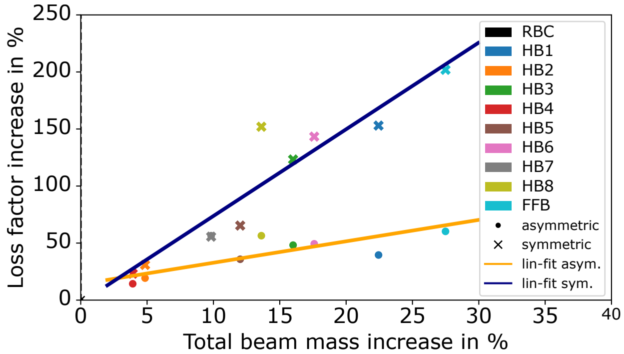

Fig. 31: Loss factor - mass gain relation in tail boom clamping test series

mode generally has a significantly poorer loss factor increase relative to the added mass. However, this is partially due to the overall higher absolute value in this mode. Qualitatively, the damping enhancements of the various beams exhibit similar behavior for both modes. HB3, HB6, and HB8 are the only ones that lie above the line for both cases. HB7 is only above the line for the asymmetrical mode. Notably efficient is the HB8 beam, featuring a sinusoidal pattern and 100% hybridization of the central web portion, albeit with only partial hybridization across the span. HB8 demonstrates an increase of plus 150% in damping with a mass increment of less than 14%.

5 HORIZONTAL STABILIZER

5.1 REFERENCE COMPONENT

The horizontal stabilizer or tailplane utilized in this study is derived from the COAX 2D ultralight helicopter by EDM Aerospace GmbH. Figure 32 displays the tail section of this helicopter. This stabilizer was selected for its uncomplicated shape, easy-to-access molds, and straightforward manufacturing. Furthermore, the aerodynamic loads on the horizontal tail of this unit are already known and were previously described by Henschel [11]. Another advantage is the presence of a reference component, which enables reference measurements and comparisons.

The horizontal stabilizer features a simple rectangular design with a constant airfoil profile. The reference is constructed using a sandwich structure and attached to the tail boom with two screws positioned one behind the other in the middle, securing it to a negative-profiled attachment point. To enhance attachment, the bottom side of the tail assembly is reinforced with a bulge around the screw

Table 12: Parameter levels and positive influence on loss factor

Parameter	Parameter Levels and Impact		
FP function	quadratic-, sinusoidal	>	linear, quadratic+
Longitudinal extent	full	>	partial
Hybridization degree	p100	>	p50
Stacking Sequence FFRP	TD-F	≈	BU-F
Stacking Sequence CFRP	TD-C	≈	BU-C

Fig. 32: Wing attachment on the CoAx 2D [27]

Fig. 33: Bulge for reinforcement around the clamping of the horizontal stabilizer

(see Figure 33). From dynamic tests that were conducted on the reference wing, it was determined that the eigenfrequency of the symmetrical bending mode is 78.4 Hz.

5.2 DESIGN & LAYUP

The design of the hybrid horizontal tail assembly was accomplished in two phases. Initially, it was sized to withstand the static loads described in Henschel [11]. Subsequently, the objective was to accurately replicate the dynamic characteristics of the reference tail assembly to ensure a valid comparison of damping values. In addition, the weight was targeted to be minimized.

As a construction method, the chosen design for the horizontal stabilizer involves a double-T spar/beam shell structure, utilizing the methods outlined by Henschel [11] and John [15]. For a

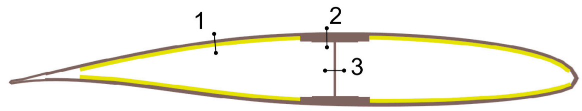

Fig. 34: Layering arrangement of the airfoil cross-section

visual representation of the stabilier's cross section, depicting the three distinct layups of the airfoil profile, refer to Figure 34. To minimize residual stresses on the fiber-reinforced composite section, a symmetrical design approach must be utilized. The layering sequence of the upper airfoil laminate is mirrored in the lower airfoil laminate to maintain symmetry.

The airfoil section's design enables a transfer of previous findings from DTB configurations. It is recommended that the airfoil center around the clamping consists mainly of flax material to achieve optimal damping rates. Thus, a 100% flax section was designed in the initial phase to be rigid enough to meet the static requirements. For the skin layers (1), John et al. [15] demonstrated that using five layers of flax fabric at a 45° angle and one layer of powerRibs™ was sufficient to withstand the aerodynamic and torsional loads. The DTB structure is a spar that primarily absorbs the shear and bending loads. Due to the design and limited space with a predetermined C-height of the DTB, a maximum of 16 layers could be accommodated. As a result, it is not possible to enhance EI by adding more layers to the flange; it can only be achieved by widening the layers. However, this comes with the disadvantage that the Steiner contribution cannot additionally contribute. The width of the flange (2) and the layer arrangement of both C-sections (3) were optimized utilizing a FEM model to ensure that the deflection is in line with the specified values for intermediate, limit, and ultimate loads from Henschel's [11] experiment.

The simulation results are compared to the experiment in Figure 35. By using the layup at position (1), (2), and (3) described in Table 13 and a maximum flange width of 31 mm, the simulation effectively fulfilled all load scenarios. Under greater loads,

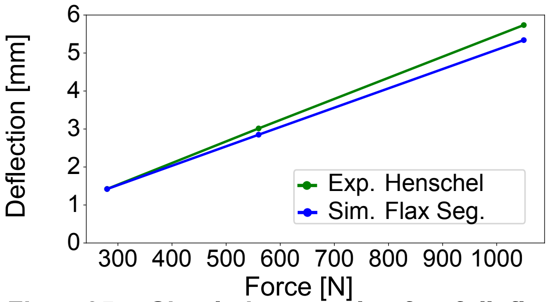

Fig. 35: Simulation results for full flax wing section vs Henschel [11]

Table 13: Layups of 100% flax airfoil cross section .

Position	Layup
1	$[FT^{\pm 45}]_5 PR$
2	$[FT^{\pm 45}]_5 [F^0]_{16} F^{45} F^{135}$
3	$[F^{45} F^{135} F0]_s$

the simulation demonstrated even greater stiffness compared to the experimental results from Henschel. This increased stiffness provides an additional level of safety in the design. The airfoil section stacking order acted as the initial basis for the subsequent optimization of the horizontal stabilizer.

The next phase involved designing for dynamic properties. This included considering both the stiffness (EI) of the flange and the distribution of mass towards the outer sections of the stabilizer. The reference horizontal stabilizer symmetrical eigenfrequency of 78,4 Hz served as the optimization target for the hybrid. Furthermore, the insights obtained from the DTBs were incorporated to attain superior damping properties. Figure 36 illustrates a simplified representation of the horizontal stabilizer's layer configuration.

Based on the findings of the DTB investigations, a sinusoidal pattern was added to the stabilizer's flange, gradually transitioning between the 100% flax web and the pure carbon flange (2). Moreover, the width of the flax material was adjusted in various sections. This technique enabled the efficient tuning of the natural frequencies through the EI distribution of the flange. The chosen transition function for the HLW is depicted in Figure 36. Following the design guidelines for carbon composites, all transition points feature a minimum step size of 10.2 mm, as per the requirement that the step distance be greater than 60 times the step size. Each flange in the DTB comprises 16 layers in a unidirectional combination of flax and carbon. The outer 15 layers exhibit a more intricate geometry for weight reduction, while the initial layer is rectangular

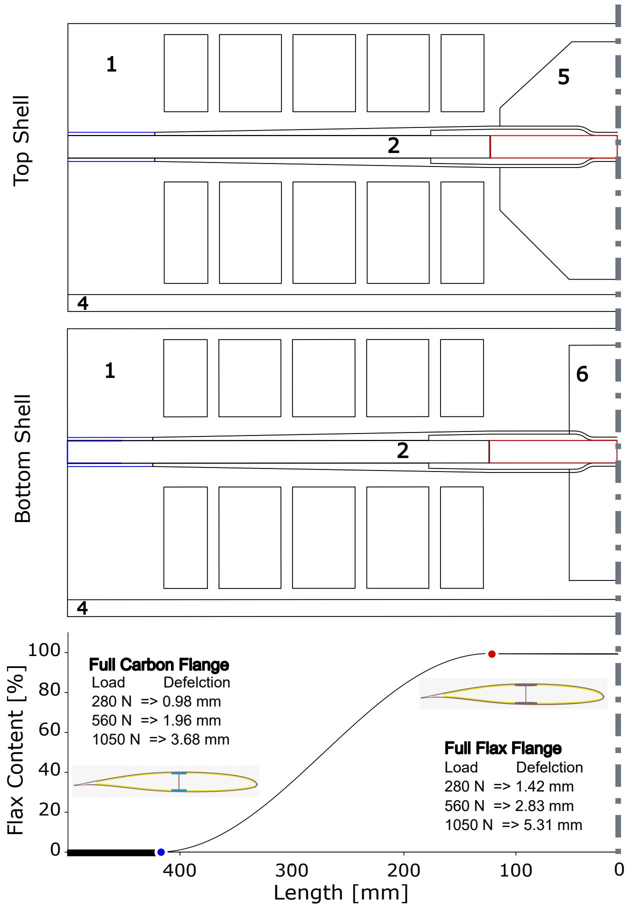

Fig. 36: Layup design of damping optimized horizontal stabilizer with positions (1),(2),(4),(5), and (6)

and as wide as the DTB (20 mm). The flange on each side has a step size of 0.2 mm in the chord direction to create a smooth transition between the layers. This results in an outermost layer of the pure flax flange at its widest cross section of 37 mm. The flange near the attachment point tapers inwards, narrowing down to a minimum width of 20 mm. This 20 mm width is also common to the 16 outermost carbon layers of the pure carbon web located at the outermost edge of the wing.

The two inner layers of the skin have rectangular cutouts to reduce the overall weight of the HLW (1). The cutouts are located between the full flax flange and full carbon flange sections to achieve the required stiffness in the center and greater mass at the wing tips. This additional weight is essential to replicate the reference wing's eigenfrequencies. The final two plies of flax are 15 mm shorter at the trailing edge than the first three to allow ample room for the seamless placement of both tools (4). The shells' bolt attachments were strengthened with carbon twill and UD layers (5,6). Particularly, the geometric bulge depicted in Figure 33 (6) requires the reinforcement as there is no support from clamping. For this purpose, an integration was performed using 8 layers of quasi-isotropic carbon twill (CT) in this section. Moreover, reinforcement was made to the joint between the two screws with unidirectional (UD) carbon material (C). To provide an enhanced load transfer from the attachment point to the rest of the wing, an octagon-shaped cut-out was created in the fourth layer of the top shell (5), filled with a patch of flax fabric (2) with +/- 90° orientation as well as two extra rectangular layers of carbon twill.

As a result, a symmetrical bending eigenfrequency of 81.68 Hz was determined in the simulation. The 3.22 Hz difference from the reference stabilizer's eigenfrequency of 78.4 Hz was retained as a safety margin to allow for potential adjustments using tuning masses. For this reason, initially, lighter and, in comparison, thinner endplates with only six layers of flax twill were designed to not add too much mass in the tailplane tips from the beginning.

5.3 MANUFACTURING & PROPERTIES

The horizontal stabilizer was manufactured in five parts: the wing's top and bottom shells, the DTB, and the two endplates. Due to the deviation of the thickness of the layers from the target value in the previous study, a pressure of 7 bar was used for the autoclave process, which corresponds to an absolute reference pressure of just under 8 bar, achieving a layer thickness of round about 1.7mm. These parts were then bonded using high-performance aerospace structural adhesive to create the final product. Figure 37 illustrates the 3D flange layer arrangement before 37a and after lamination 37b. Both figures display the sinusoidal hybridization pattern. To create a durable adhesive surface, a 3 mm flange was added to the end of the wing by laminating it around the edges of the tailplane mold. The endplates were then bonded during the final stage of the process. Figure 38 shows the visual details of the endplate attachment.

The completed assembly is shown in Figure 39, while Figure 40 provides a detailed view of the tailplane attachment area on the underside.

Both stabilizers were measured and weighed. The properties of the two are summarized in Table 14. Only the wingspan differs just under a millimeter due to the narrower endplates; however, the dimensions are the same for both stabilizer. The total weight of the hybrid is 1202 g, which is approximately 5% heavier than the reference, which weighs 1148

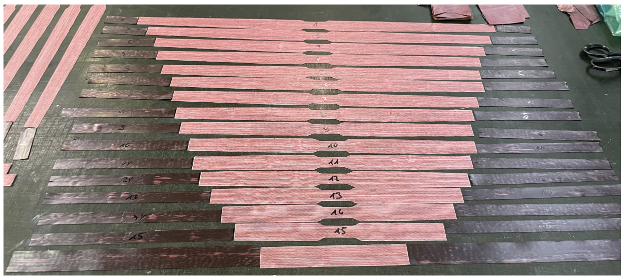

(a) Prepregs of Flange before the layup

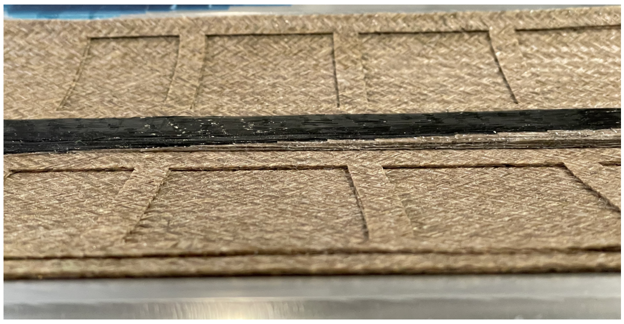

(b) Sinus curve visible in flange layup

Fig. 37: Description of the Flange Layup

Fig. 38: Closeup of the hybrid horizontal stabilizer endplates

g. Considering tuning weight of 27.5 g, which is approximately equivalent to thickened endplates of 1.2 mm of flax, the hybrid stabilizer has a weight of 1257 g, representing a 9.4% increase from the reference.

5.4 DYNAMIC ANALYSIS

5.4.1 Clamping Condition & Test Procedure

To clamp the horizontal stabilizer's curved surfaces, a negative counterpart of the airfoil shape was crafted from monolithic carbon, similar to the attachment used in the original helicopter. The attachment is depicted in Figure 41. The mold's thickness varied from 5 mm in the center to 10 mm on the leading and trailing edge. An aluminum plate measuring

Fig. 39: Final assembly of the hybrid horizontal stabilizer next to the reference

10 mm in thickness was affixed to this surface with aviation adhesive, serving as the fixing point for the dynamic measurements. The same fixing apparatus was utilized for both stabilizers.

Both horizontal stabilizers were measured using the setup outlined in Figure 1. Three measurement points and two excitation points were utilized on each of the sides of the tailplane. The flange features two excitation points split between the inner and outer sides of the wing. The third point of measurement is placed on the outer side of the horizontal stabilizer,

Fig. 40: Attachment area on the underside of the hybrid horizontal stabilizer

Table 14: Properties of hybrid and reference horizontal stabilizer

	Hybrid	Reference
Wing Span	987 mm	989 mm
Chord Length	24.9 mm	24.9 mm
Endplate thickness	1.49 mm	2.76 mm
Complete Weight	1202 g	1148 g
Bottom Shell	540 g	-
Top Shell	505 g	-
DTB	63 g	-
Endplate	2 *x* 25 g	-
Adhesive	44	-

Fig. 41: Clamping condition horizontal stabilizer

positioned specifically at the shear center to minimize potential effects from excited torsional modes.

In total, there are 24 different measurement combinations for each stabilizer configuration. The hybrid was assessed both with and without tuning masses. Each tuning mass weighed 27.5 g per side, equivalent to the calculated extra weight of the thicker endplates of the reference. The study focused on the first and second bending modes of the specimen, similarly to the DTB investigations.

5.4.2 Results

From the collected FRFs, the HPM determined the natural frequencies and modal dampings. Figure 42 displays one of the FRFs obtained for all three stabilizer configurations, including carbon reference and hybrid with and without tuning mass. The natural frequencies of the hybrid stabilizer without added tuning masses are higher than those of the carbon reference, whereas the configuration with additional mass closely matches the eigenfrequencies. Table 15 summarizes all of the achieved eigenfrequencies for the three configurations and the corresponding simulated values.

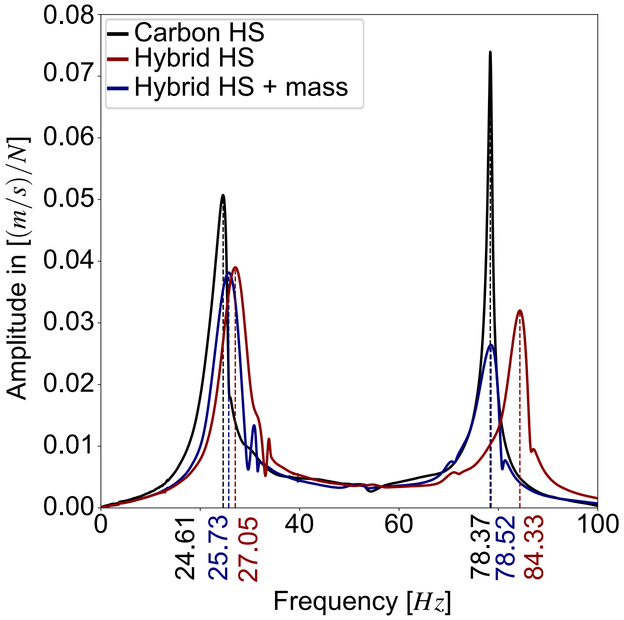

Fig. 42: Comparison of one example set of FRFs for reference and hybrid horizontal stabilizer with and without tuning mass

Table 15: Eigenfrequencies of different horizontal stabilizer configurations

	ω_1 in Hz	ω_2 in Hz	weight in g
Carbon HS	25.31	78.46	1149
Hybrid HS Sim.	66.15	81.68	1288
Hybrid HS Exp.	27.95	84.97	1202
Hybrid HS Exp. (+ mass $2\ x\ 27.5\ g$)	25.82	78.26	1257

When comparing the simulated second eigenfrequency ω_2 with the measured one, it becomes apparent that the simulated value is higher than expected, above the planned safety margin that was implemented to allow for potential downward adjustments if needed. Comparing the weights of the hybrid in the simulation and the one produced, it is clear that the simulated weight is considerably greater. This indicates that more resin may have been extracted during production than anticipated, resulting in a lighter horizontal stabilizer and a subsequent rise in frequency.

Examining the first eigenfrequency ω_1 from the simulation with the experimental result reveals an even larger discrepancy. The significant difference suggests an incorrect boundary condition in the simulation, which affects only the asymmetrical eigenfrequency. With the assistance of the added mass, it becomes evident that the natural frequencies could be accurately matched. For the symmetrical mode, the deviation is less than 1%, and for the asymmetrical mode, it is less than 5%. Considering this, the total mass of the hybrid structure from the experiment remains still lighter than the simulated value.

The results of the loss factors across the frequency range are presented in Figure 43. The mean value for each mode is represented as a point, accompanied by the standard deviation over the different measurements. A significant contrast in the damping between the first (asymmetrical) bending mode and the second (symmetrical) bending mode is apparent. The asymmetrical bending mode exhibits remarkably high loss factors for both the hybrid and reference horizontal stabilizer. This behavior for the asymmetrical mode was already observed in DTBs. Just like there, it is reasonable to assume that various effects are at play that cause the damping to increase significantly beyond the structural damping of the materials. The standard deviation also illustrates this with a high dispersion bewteen the single measurements. Undoubtedly, a significant part of this behavior is due to the clamping. Friction and shear flexibility contribute significantly to the increased damping. A mounting that extends beyond the centerline or a wider contact area should help reduce this effect. However, as with the case of the DTBs, a qualitative difference between the damping of the hybrid and the reference can still be demonstrated.

On the other hand, the symmetrical mode shows almost no scatter in the data points, neither in the loss factor nor in the frequency. The standard deviation is very small. In a quantitative comparison with the DTBs, the damping is higher. The carbon reference achieves a loss factor of 1.06. The tuned hybrid beam achieves a loss factor of 4.64. This has further increased the disparity between the two from about 2.5 (HB8) to 4.2. This is due in part to the even higher flax content (now 100% in the cross section at the attachment point and in the web) and the additional 45° BD layers in the skin.

Comparing the loss factors with and without tuning masses, the symmetrical mode shows a further increase in damping despite the trend of increasing damping over rising frequency observed in the DTB series. This may indicate the presence of nonlinearities in the damping. One way to further investigate this direction is to use a shaker or various levels of impact to examine the component for nonlinear behavior. An evaluation of this data is currently pending.

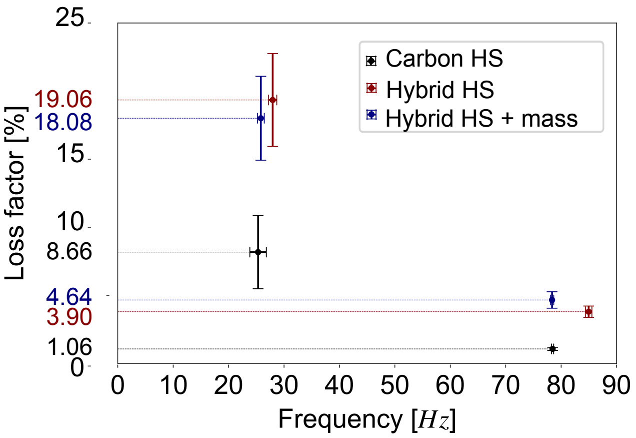

Fig. 43: Comparison of the eigenfrequencies and the corresponding loss factor between the carbon reference and the hybrid horizontal stabilizer with and without tuning mass.

6 CONCLUSION & OUTLOOK

This study aimed to investigate the impact of hybridisation on the damping properties of a composite component, such as a helicopter horizontal stabilizer, using three-dimensionally arranged carbon fibres and flax fibre-reinforced polymers. This concept was first investigated in the form of Double-T beams (DTB)s because they are a representative aerospace structure and can replicate key features of the properties of a horizontal stabilizer in a simplified manner. Furthermore, the results were applied on a horizontal stabilizer from a ultra light helicopter. In conclusion, the findings suggest the following:

1. Symmetrical and asymmetrical modes were identified for all the structures examined. However, it seems that the damping values for the asymmetrical modes are heavily influenced by other effects. In contrast, the data obtained for the symmetrical modes were very consistent, indicating that the damping for the second eigenmode could be reliably determined.
2. The DTB test series results indicate that hybridization with flax fibers can significantly increase the loss factors of the symmetrical bending mode. High hybridization in the high strain regions is necessary for this effect. The progression of hybridization across the span should not occur too rapidly. A sinusoidal pattern has proven to be the most effective regarding the damping over weight increase.
3. The predictive ability of the horizontal stabilizer's natural frequencies was found to be satisfactory. Predictions of natural frequencies were successfully achieved and properly optimized.
4. The findings from the DTB research were successfully utilized in enhancing the horizontal stabilizer. The dynamic analysis confirmed that a hybrid helicopter structure can achieve similar dynamic properties as a carbon reference while having significantly improved damping capabilities. The loss factor of the first symmetric bending mode increased from 1.06% to 4.64%, resulting in a more than fourfold improvement at the same frequency. The increase in mass was less than 10%, rendering the concept competitive with common damping methods.

The results indicate that the damping due to flax fibers may be subject to nonlinearities. For future work a shaker will be used for an amplitude-dependent examination. Optical measurements will also be conducted to extend measurements to a full Experimental Modal Analysis (EMA). An experimental investigation of the failure criteria of the tailplane is still pending to also ensure its resilience against failure.

Author contact:
Jonas John, jonas.john@tum.de
Lukas Gaugelhofer, Lukas.gaugelhofer@tum.de
Ilkay Yavrucuk, ilkay.yavrucuk@tum.de

7 ACKNOWLEDGMENTS

This work is supported by the German Federal Ministry for Economic Affairs and Climate Action through the German Aviation Research Program LuFo VI-1 in the project eVolve.

Supported by:

Federal Ministry
for Economic Affairs
and Climate Action

powerRibs™ is a registered trademark of the company BCOMP®

8 REFERENCES

[1]Datta, A., *Fundamental understanding, prediction and validation of rotor vibratory loads in steady-level flight*, University of Maryland, College Park, 2004.

[2]Braun, “Development of antiresonance force isolators for helicopter vibration reduction,” *Journal of the American Helicopter Society*, Vol. 27, (4), 1982, pp. 37–44.

[3]H. Rottmayr, W. Popp, and R. Mehlhose, editors, Application of modern vibration control techniques on EC135 and future trends , 1997.

[4]M. Rinker, T. Ries, M. Embacher, S. Platzer, G. Uhl, and M. Hajek, editors, Simulation of Rotor–Empennage Interactional Aerodynamics in Comparison to Experimental Data , 2019.

[5]K. e. a. Frederickson, editor, Experimental investigation of main rotor wake induced empennage vibratory airloads for the RAH-66 Comanche helicopter . AMERICAN HELICOPTER SOCIETY, 1993.

[6]Schaeferlein, U., Keßler, M., and Kraemer, E., “Aeroelastic simulation of the tail shake phenomenon,” *Journal of the American Helicopter Society*, Vol. 63, (3), 2018, pp. 1–17.

[7]Leishman, G. J., *Principles of helicopter aerodynamics with CD extra*, Cambridge university press, 2006.

[8]Sheridan, P. F., and Smith, R. P., “Interactional aerodynamics—a new challenge to helicopter technology,” *Journal of the American Helicopter Society*, Vol. 25, (1), 1980, pp. 3–21.

[9]A. Kus, S. Schneider, M. Hollands, R. Rammer, O. Dieterich, and M. Priems, editors, GRC1: An Advanced Five-Bladed Bearingless Main Rotor Dynamics and Acoustics from Draft to Flight Test , 2018.

[10]Yang, J., Xiong, J., Ma, L., Wang, B., Zhang, G., and Wu, L., “Vibration and damping characteristics of hybrid carbon fiber composite pyramidal truss sandwich panels with viscoelastic layers,” *Composite Structures*, Vol. 106, 2013, pp. 570–580.

[11]Henschel, K. A., *Biocomposites in Aviation Structures on the Example of Flax and its Hybrids*, Ph.D. thesis, Technische Universität München, 2020.

[12]Karus, M., and Kaup. M., “Naturfasern für die europäische Automobilindustrie,” , 2002.

[13]K. Strohmann and M. Hajek, editors, An Eco-Efficient Helicopter Tailplane Hybridized from Flax, Balsa and Carbon , 2019.

[14]J. John, L. Gaugelhofer, and M. Hajek, editors, Increasing the Damping Properties of Carbon Laminates by Flax Fiber Hybridization for Rotorcraft application , 2022.

[15]J. John, L. Gaugelhofer, M. Hajek, and I. Yavrucuk, editors, Increasing Damping Properties of Helicopter Composite Substructures using Flax Fiber Hybridization , 2023.

[16]L. Gaugelhofer, J. John, I. Yavrucuk, and M. Hajek, editors, Experimental Investigation of Tensile Properties of Flax Fiber Reinforced Composites , 2022.

[17]ASTM, “Standard Test Method for Measuring Vibration-Damping Properties of Materials,” , 2017.

[18]Mohanty, P., and Rixen, D. J., “Operational modal analysis in the presence of harmonic excitation,” *Journal of Sound and Vibration*, Vol. 270, (1-2), 2004, pp. 93–109.

[19]Mohanty, P., and Rixen, D. J., “Modified ERA method for operational modal analysis in the presence of harmonic excitations,” *Mechanical Systems and Signal Processing*, Vol. 20, (1), 2006, pp. 114–130.

[20]Rex, W., *Output-Only Aeroelastic Analysis of Helicopters in Atmospheric Turbulence*, Ph.D. thesis, Technische Universität München, 2021.

[21]Comsol, “Eigenfrequency Analysis,” , Apr. 2018.

[22]Giurgiutiu, V., *Stress, Vibration, and Wave Analysis in Aerospace Composites: SHM and NDE Applications*, Academic press, 2022.

[23]Schürmann, H., *Konstruieren mit Faser-Kunststoff-Verbunden: Mit 39 Tabellen*, VDI-/Buch], Springer, Berlin and Heidelberg, second edition, 2007.

[24]Mukherjee, A., and Varughese, B., “Design guidelines for ply drop-off in laminated composite structures,” *Composites Part B: Engineering*, Vol. 32, (2), 2001, pp. 153–164.

[25]Klein, B., *Versuchsplanung—DoE: Einführung in die Taguchi/Shainin-Methodik*, Oldenbourg Verlag, 2011.

[26]Lee, J. W., and Lee, J. Y., “Free vibration analysis using the transfer-matrix method on a tapered beam,” *Computers & Structures*, Vol. 164, 2016, pp. 75–82.

[27]“UL-Hubschrauber COAX 2,” https://www.aerokurier.de/motorflug/kleiner-thueringer-ul-hubschrauber-coax-2/, 20.08.2023, 2024.